

Faraday Discussions

Accepted Manuscript



This manuscript will be presented and discussed at a forthcoming Faraday Discussion meeting. All delegates can contribute to the discussion which will be included in the final volume.

Register now to attend! Full details of all upcoming meetings: <http://rsc.li/fd-upcoming-meetings>



This is an *Accepted Manuscript*, which has been through the Royal Society of Chemistry peer review process and has been accepted for publication.

Accepted Manuscripts are published online shortly after acceptance, before technical editing, formatting and proof reading. Using this free service, authors can make their results available to the community, in citable form, before we publish the edited article. We will replace this *Accepted Manuscript* with the edited and formatted *Advance Article* as soon as it is available.

You can find more information about *Accepted Manuscripts* in the [Information for Authors](#).

Please note that technical editing may introduce minor changes to the text and/or graphics, which may alter content. The journal's standard [Terms & Conditions](#) and the [Ethical guidelines](#) still apply. In no event shall the Royal Society of Chemistry be held responsible for any errors or omissions in this *Accepted Manuscript* or any consequences arising from the use of any information it contains.

A classical treatment of optical tunneling in plasmonic gaps: extending the quantum corrected model to practical situations[†]

R. Esteban,^{a,b} A. Zugarramurdi,^{c,d} P. Zhang,^{e,f} P. Nordlander,^g
F. J. García-Vidal,^{b,f} A. G. Borisov^{b,c} and J. Aizpurua^{*a,b}

Received Xth XXXXX 20XX, Accepted Xth XXXXX 20XX

First published on the web Xth XXXXX 200X

DOI: 10.1039/c000000x

The optical response of plasmonic nanogaps is challenging to address when the separations between the two nanoparticles forming the gap is reduced to a few nanometers or even subnanometer distances. We compare results of the plasmon response within different levels of approximation, and identify a classical local regime, a nonlocal regime and a quantum regime of interaction. For separations of a few Ångströms, in the quantum regime, optical tunneling can be produced modifying strongly the optics of the nanogap. We consider a classical effective model, so called Quantum Corrected Model (QCM), that has been introduced to correctly describe the main features of optical transport in plasmonic nanogaps. The basics of this model are explained in detail, and its implementation is extended to include nonlocal effects and address practical situations involving different materials and temperatures of operation.

1 Introduction

Surface Plasmon Polaritons, the collective oscillations of free electrons that are excited resonantly in metals by an optical electromagnetic field, can be localized in finite structures acting as optical nanoantennas. The resulting Localized Surface Plasmon Polaritons (LSPPs) allow manipulating light at the nanoscale and obtaining strong and very confined local field enhancements^{1–6}. This opens

^a Materials Physics Center CSIC-UPV/EHU, Paseo Manuel de Lardizabal 5, 20018, Donostia-San Sebastián, Spain, Fax: 34 94301 5800; Tel: 34 94301 8830; E-mail: aizpurua@ehu.es

^b Donostia International Physics Center DIPC, Paseo Manuel de Lardizabal 4, 20018, Donostia-San Sebastián, Spain

^c Institut des Sciences Moléculaires d'Orsay, UMR 8214, CNRS-Université Paris-Sud, France

^d COMP, Department of Applied Physics, Aalto University, P. O. Box 11100, FIN-00076 Aalto Espoo, Finland

^e Department of Photonics Engineering, Technical University of Denmark, DK-2800 Kgs. Lyngby, Denmark

^f Departamento de Física Teórica de la Materia Condensada, Universidad Autónoma de Madrid, E-28049 Madrid, Spain

^g Department of Electrical and Computer Engineering, MS378, Laboratory of Nanophotonics, Rice University, Houston Texas 77005, USA

a route to a variety of applications, in e.g. Surface Enhanced Raman Spectroscopy (SERS)^{7–11}, control of radiation from single quantum emitters^{12–17}, or generation of high harmonic pulses at extreme ultraviolet frequencies via non-linear processes¹⁸. The optical response of many plasmonic systems^{3,4,7–9,19–22} has been successfully addressed using Maxwell' Equations. Within this classical approach different materials are separated by sharp boundaries and the material properties are given by the position and frequency dependent dielectric function $\epsilon(\mathbf{r}, \omega)$. Within the local, linear dielectric response, we can relate the dielectric displacement \mathbf{D} and the electric field \mathbf{E} at a position \mathbf{r} through $\mathbf{D}(\mathbf{r}, \omega) = \mathbf{E}(\mathbf{r}, \omega) + 4\pi\mathbf{P}(\mathbf{r}, \omega) = \epsilon(\mathbf{r}, \omega)\mathbf{E}(\mathbf{r}, \omega)$, where the medium polarisation \mathbf{P} verifies $4\pi\mathbf{P}(\mathbf{r}, \omega) = (\epsilon(\mathbf{r}, \omega) - \mathbf{1})\mathbf{E}(\mathbf{r}, \omega)$ (in atomic units). Equivalently, $\mathbf{P}(\mathbf{r}, \omega) = \chi(\mathbf{r}, \omega)\mathbf{E}(\mathbf{r}, \omega)$, where $\chi(\mathbf{r}, \omega) = (\epsilon(\mathbf{r}, \omega) - \mathbf{1})$ is the medium polarisability. For an isotropic and homogeneous medium, ϵ and χ can be described as scalars, while in the general case these are tensors of rank 2. The described linear relationship between \mathbf{E} and \mathbf{P} excludes possible non-linearities that occur for strong fields^{23–25}, and it only depends on the particular point of evaluation \mathbf{r} .

Among the different plasmonic configurations, gap-nanoantennas composed by two metal particles separated by a narrow dielectric gap [as those schematically depicted in Fig. 1(a) and Fig. 1(b)] are particularly interesting as they serve to probe many fundamental optoelectronic processes in the nanoscale. The local classical approach of metallic nanogaps predicts that arbitrarily large charge densities can be induced at the opposite sides of a vanishingly narrow plasmonic gap, leading to extremely intense fields at the gap^{3–5,7–9,19–22,26,27} and to strongly redshifted hybridized bonding LSSP resonances that arise from Coulomb coupling between the modes. The lowest energy gap mode is known as Bonding Dimer Plasmon (BDP) and its redshift with narrowing gap is usually a good fingerprint of the plasmonic cavity^{21,22,28–32}. Within the local classical treatment, the transition from the separated to the overlapping nanoparticles is characterised by the discontinuity of the energy of the resonances, with a sharp change of the optical response at the touching point. After contact, a set of Charge Transfer Plasmons (CTPs) that blueshift with increasing overlap appears.^{21,29,33,34} This behaviour is outlined by the solid blue lines in Fig. 1(c).

Local classical treatments, however, disregard nonlocal and quantum effects^{35,36} that lead, for example, to the size dependence of the plasmon energy of individual nanoparticles^{37–45}. In addition to quantum-size effects, the complex quantum interactions between electrons can also change dramatically the optical response of very narrow, nanometer and subnanometer gaps, a regime progressively available for experimental test, where the limitations of classical descriptions are manifested^{46–55}. A local classical description of the response of metallic nanoparticles does not properly account for the correlated motion of the conduction electrons and their spill out the nanoparticle surfaces. Thus, the classical local model fails to capture (i) the finite spatial profile of the screening charge⁵⁶ with smooth transition of the electron density at the interfaces, instead of sharp discontinuities, (ii) strong nonlocal interactions so that, in general, the centroid of the screening charge density does not coincide with the geometrical interface, (iii) tunneling between the metal nanoparticles particles, where the conductive contact can be established prior to the direct geometrical contact.

To be able to capture these effects, one possibility is to perform rigorous

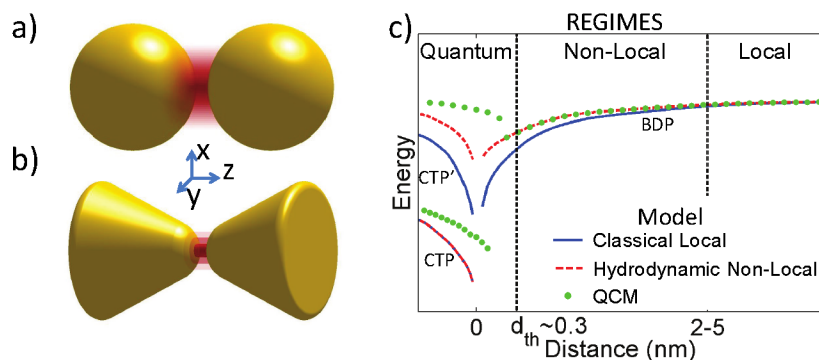


Fig. 1 General consideration of quantum effects and the Quantum Corrected Model (QCM). (a,b) Example of the implementation of the QCM in metallic gaps. In (a) a spatially inhomogeneous effective medium whose properties depend continuously on the separation distance is introduced in the gap between two metallic spheres. (b) considers a bow-tie plasmonic nanoantenna where the effective medium in the gap is described by a set of discrete homogeneous shells of effective material. Each of these shells is characterized by a constant permittivity that corresponds to a representative local separation distance. The permittivity always remains constant in the longitudinal z direction along the axis of the dimers, and only changes in the horizontal xy plane. c) Sketch of the evolution of the resonant wavelength of the Bonding Dimer Plasmon (BDP) and two Charge Transfer Plasmons (CTP and CTP') of a metallic dimer in vacuum. Three different interaction regimes can be distinguished: a classical local regime ($d \gtrsim 2 - 5$ nm), a classical nonlocal regime ($0.3 - 0.4$ nm $\lesssim d \lesssim 2 - 5$ nm), and a quantum regime ($d \lesssim 0.3 - 0.4$ nm). Results of a local treatment (solid blue line), a nonlocal hydrodynamical model (dotted red line) and the Quantum Corrected Model (black solid dots) are displayed.

quantum mechanical calculations of the optical response using the Time Dependent Density Functional Theory (TDDFT)^{34,57–61}. In contrast to the classical calculations, quantum results for very narrow gaps show pronounced effects of the electron tunneling such as a strong reduction of the field enhancement, a continuous transition of modes between the non-touching and contact regimes and the appearance of a Charge Transfer Plasmon (CTP) mode before the nanoparticles touch^{33,62}. These effects are outlined by dotted green lines in Fig. 1(c).

Full-quantum approaches are very useful to understand the physics involved but show limitations when trying to model realistic materials and structures. Because of the heavy computational load, only relatively small structures could be addressed so far. For example, using a free-electron jellium description of the metal allows simulating systems of a few thousand electrons, corresponding to dimensions of only a few nanometers. Attempting the full atomistic approach further reduces the feasible size of the system to several hundreds of electrons⁶³. In contrast, typical plasmonic systems are much larger and can easily contain many millions of electrons. It is thus worthwhile to invest the theoretical effort to elaborate approximate methods that effectively account for nonlocal and quantum effects and allow for efficient computational schemes.

During the last years, different models have been developed where nonlocal effects were accounted for with model dielectric functions, or within the

theory of surface screening^{2,64–73}. The nonlocal hydrodynamical (NLHD) description has attracted considerable interest because of its numerical efficiency for arbitrarily-shaped objects^{47,74–84} and the possibility to obtain semi-analytical solutions using transformation optics⁸⁵. The introduction of nonlocality via the standard NLHD model produces a blueshift of the plasmonic modes with respect to the local classical solution, as schematically depicted with the dotted red line in Fig. 1(c). The NLHD results are adequate for metals such as silver and gold whose optical response is significantly affected by *d*-electrons, but the blueshift obtained for simple free-electron metals is in contradiction with full quantum results^{86,87}. Some approaches have proposed to recover nonlocal results by a convenient rescaling of the local distances^{86,87} and thicknesses⁸⁸ at the metal interfaces, providing good descriptions of the plasmon energies and dispersions in nanometric gaps. Recently, the inclusion of the realistic density profile above the surface into the NLHD description allowed to retrieve the full quantum and experimental results both for *d*-electron and simple metals⁸⁹, at the price of the increased computational cost. While the above treatments address the nonlocal screening, it is only recently that the charge transfer between the particles due to quantum tunneling could be accounted for within a classical treatment appropriate for large systems. The Quantum Corrected Model⁶² (QCM) was introduced to account for the tunneling current across the gap via the insertion of an effective conductive medium in the gap [red areas sketched in the dimers of Fig. 1(a) and Fig. 1(b)]. The conductivity of this effective medium is set from the electron transmission properties of the interparticle barrier. The method was first successfully tested against TDDFT calculations of the optical response of nanogaps of small particles⁶², and latter used to interpret experimental results for subnanometric realistic gaps^{46,90}.

As sketched in Fig. 1(c), we can distinguish between three different separation distance regimes in plasmonic gaps. The classical regime corresponds to wide gaps, down to a separation that depends on the size of the particles but can be estimated as $\sim 2 - 5$ nm, where a classical local approach gives basically the same results as nonlocal treatment. We identify this range of large separations as a local classical regime. As the gap becomes smaller, both local and nonlocal classical descriptions predict a similar qualitative behaviour: continuous redshift of plasmonic modes and rise of the near fields. However, quantitative differences emerge, as observed in Fig. 1(c). We thus define the range of separation distances below $\sim 2 - 5$ nm down to $\sim 0.3 - 0.5$ nm as the one corresponding to strong nonlocal effects. For separation distances below $\sim 0.3 - 0.5$ nm the electron tunneling between the nanoparticles quenches the strong charge concentration across the gap and thus critically affects the plasmonic response⁶⁰. This pure quantum effect can become significant even for larger distances under intense lasers³⁴. We thus identify a third range of plasmonic gaps size, below $\sim 0.3 - 0.5$ nm, where pure quantum effects take over. As depicted in Fig. 1(c), in this quantum regime the electron tunneling leads to a gradual transition from modes that red-shift towards modes that blue-shift with narrowing gaps (left hand side of the figure). The three ranges of distances identified in this introductory figure correspond to the three levels of theoretical modeling required to correctly address the optical response of the strongly interacting plasmonic nanogap system.

The objective of this paper is to discuss comprehensively the QCM as a

method that can incorporate quantum effects and in particular electron tunneling in many practical situations of interest. Notably, the QCM has typically used a local framework, but can incorporate nonlocality as demonstrated for 2D-particles⁹¹. Here, we develop a nonlocal QCM that we apply to dimers of realistic size. We analyze the plasmonic response with and without inclusion of nonlocality and/or tunneling to reveal the relative importance of each contribution for gaps of different sizes. This is highly relevant for the interpretation of experimental data obtained in plasmonic nanogap systems.

In the following, we first describe the technical details of the QCM^{46,62}, and discuss the relevance of the long-range image charge interactions for the correct description of the electron tunneling barrier. We detail the step-by-step procedure to define the effective medium required in the QCM for the case of arbitrary metals surrounded by a dielectric. We also show how nonlocality can be incorporated into the model. We then discuss local classical, nonlocal classical, local QCM and nonlocal QCM results of the optical response of Au dimers to identify separately the effects of tunneling and nonlocality. Last, we discuss the implementation of the QCM for different materials, and consider the influence of temperature. Throughout the paper atomic units are used unless otherwise stated.

2 Implementation of the local QCM

In this section, we first describe the quantum mechanical calculation of the static tunneling between two closely located metallic surfaces (subsection 2.1). The metal-to-metal tunneling barrier is obtained within the simple Jellium model (JM) description of the leads. A typical Scanning Tunneling Microscopy (STM) approach is then used to obtain the conductance of the junction (subsection 2.2). Within the JM the metal is described as a gas of interacting electrons moving in a uniform positive background charge representing ionic cores. The interface between the background charge and the vacuum defines the so-called jellium edge that delimits the free electron system. For the flat metal surfaces the jellium edge is located in front of the surface atomic layer at a distance typically given by half the separation between successive atomic planes in the direction perpendicular to the surface. Under the assumption of a linear potential drop across the gap, the calculated conductance yields the static conductivity. Despite its simplicity, the JM captures the collective plasmonic modes of the conduction electrons at surfaces, in individual nanoparticles and nanoparticle dimers^{56,59,60,92}. The JM has also been successfully used to model effects associated with conduction electrons in a variety of metallic systems such as in electronic and optical properties of metal clusters and surfaces^{93–96}, charge transfer reactions between atoms and surfaces⁹⁷, conductances of molecular junctions⁹⁸, and strong-field effects.⁹⁹

The second part of this section will discuss the basis of the QCM, i.e., how to incorporate the optical conductivity derived from a quantum mechanical calculation into the classical calculations of the plasmonic response (subsection 2.3). Upon the adiabatic assumption, typical for the description of the strong field ionisation in atomic and molecular physics^{100–102}, the static conductivity (obtained quantum mechanically) is extended towards optical frequencies via a simple Drude model. We initially consider free electron metals in vacuum, but the more general scenario incorporates the contribution of the *d*-electrons to the re-

sponse of the metal and the presence of an arbitrary dielectric as surrounding medium (subsection 2.4).

The key aspect of the QCM with respect to previous classical models is the introduction of an effective medium of adequate permittivity (that relates to the optical conductivity) at the gap between metallic interfaces, to account for the possibility of charge transfer across the gap. Significantly, the definition of the effective medium incorporates the resistive nature of the gap impedance. This effective material can then be inserted into a conventional solver of the Maxwell's equations to obtain the optical response for an arbitrary geometry (subsection 2.5).

We notice that the QCM is compatible with different quantum approaches, as the only input needed is the conductivity of the junction, which can be obtained with use of a jellium model of the metal nanoparticles, or with a full atomistic description. Atomistic studies⁶³ of plasmonic dimers have pointed out some quantitative differences with respect to the jellium model for small clusters, but the main trends of the results are qualitative similar.

2.1 Electron tunneling

For typical plasmonic systems, where the size of the gap between the nanoparticles is much smaller than the radius of curvature, the local geometry of the junction can be approximated as two flat semi-infinite parallel metallic surfaces separated by a dielectric gap of size ℓ . To calculate the energy Ω - and separation ℓ -dependent electron transmission $T(\Omega, \ell)$ through the potential barrier between the flat free-electron metal leads we use a wave packet propagation method detailed previously¹⁰³. Briefly, a "probe" electron wave packet is launched from inside of one of the metal leads onto the junction. The transmitted and reflected electron fluxes are collected in two virtual detectors placed in the asymptotic regions so that the transmission T and reflection R coefficients can be extracted. Because of the symmetry of the model system, we consider only the electron motion along z , the direction perpendicular to the surfaces. The one-dimensional time-dependent Schrödinger equation, describing the evolution of the "probe" electron wave packet, is then directly solved on a grid of equidistant points.

The potential acting on the conduction electrons in the system is derived by transforming the well established model potentials proposed in Ref.¹⁰⁴. Specifically, a constant potential inside the metal is imposed, which is consistent with the JM description. As a result of this simplification, the effects of a contact between particular crystallographic faces⁶³ cannot be addressed. However, for realistic plasmonic system the contact area is rather large so that the contact can be assumed to occur between poly-crystal surfaces rather than mono-crystalline ones. Provided that the pertinent parameters such as the surface work function are set from empirical data, the JM is well suited for the description of the electric field-induced inter-particle tunneling of conduction electrons across the ultra small plasmonic junction. Note that the use of the JM is not a limitation of the QCM. The properties of the effective medium that fills the gap could be derived on the basis of full atomistic quantum calculations provided their feasibility.

The explicit form of the model potential for the electron interaction with a

semi-infinite metal surface is given by:

$$V_s(z - z_{im}) = \frac{\exp(-\xi(z - z_{im})) - 1}{4(z - z_{im})}, \quad z > z_{im}, \quad (1)$$

$$-\frac{U_0}{A \exp(B(z - z_{im})) + 1}, \quad z \leq z_{im}, \quad (2)$$

where the U_0 , z_{im} , and ξ parameters are set as in Ref.¹⁰⁴ for (111) metal surfaces. For Na we can use the tabulated data for the (110) surface (see data summarized in Table 1) or the potential calculated with density functional theory for a spherical dimer³⁴. The numerical values for A and B can be obtained by requiring continuity of the potential and its derivative at $z = z_{im}$. Within the JM of metal the tunneling barrier is mainly determined by the vacuum part of the interface potential, thus the calculated transmission of the junction is robust with respect to the choice of the surface orientation.

	$U_0(\text{eV})$	$\xi (a_0^{-1})$	$\phi(\text{eV})$	$(z_g - z_{al})(a_0)$	$(z_{im} - z_{al})(a_0)$
Ag	9.64	1.17	4.56	2.215	2.22
Au	11.03	1.33	5.55	2.225	2.14
Cu	11.89	1.27	4.94	1.97	2.11
Na	6.1	1.0	2.9	1.52	2.12

Table 1 Jellium model potential parameters: work function ϕ , jellium edge z_g and image plane position z_{im} with respect to the surface atomic layer z_{al} for different metals. Values are given in units of Bohr radius, $1 a_0 = 0.529 \text{ \AA}$

For an electron on the vacuum side above the surface ($z > z_{im}$), the potential V_s given by eqn.(1) converges to the classical attractive image potential, which is of paramount importance for the correct description of the tunneling barrier^{60,105,106}. When two metal surfaces are brought in front of each other, the image potential has to be corrected by the inclusion of the multiple images term $V_{mi}(z)$ accounting for the cross terms in the screening interactions:^{105,106}

$$V_{mi}(z) = \frac{1}{4} \sum_{n=1}^{\infty} \left\{ \frac{-1}{(z - z_{im}^{(l)}) + nZ} + \frac{-1}{(z - z_{im}^{(r)}) + nZ} \right\}, \quad z_{im}^{(l)} \leq z \leq z_{im}^{(r)}, \quad (3)$$

where the indexes (l) and (r) stand for the left and right metal surface, respectively. For z inside the metals, $z < z_{im}^{(l)}$ or $z > z_{im}^{(r)}$, the multiple image term vanishes $V_{mi}(z) = 0$.

Table 1 connects the position of the image plane z_{im} and jellium edge z_g to the position of the surface atomic layer z_{al} . The distance ℓ between the two surfaces is given by the separation between their jellium edges $\ell = z_g^{(r)} - z_g^{(l)}$, thus defining the contact at $\ell = 0$. In this section we will give a detailed description of the results obtained for an Au-Au junction, but Table 1 also gives the parameters of the model for Ag and Cu.

Finally, the total potential accounting for the long-range image-potential tail of the electron-surface interaction is given by

$$U(z) = V_s(z - z_{im}^{(l)}) + V_s(z_{im}^{(r)} - z) + V_{mi}(z) \quad (4)$$

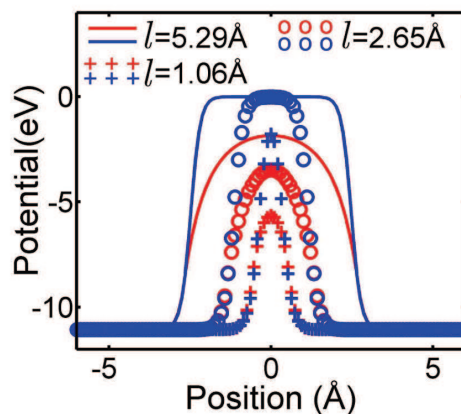


Fig. 2 Quantum-mechanical input to the QCM. (a) Potential across the gap for several values of separation ℓ as a function of position along z , where the zero position corresponds to the gap center. The results are obtained for gold surfaces separated by vacuum when considering long range interactions in the potentials given by image charges [eqn. (3) and eqn. (4)] (red lines) and without considering these long range interactions within the DFT LDA (blue lines).

In order to illustrate the role of the long-range image-charge interactions we occasionally use the effective one electron potential $U^{1e}(z)$ as derived from the density functional theory (DFT) studies within the local density approximation (LDA). In this case we perform the static DFT calculations of a plasmonic dimer formed by spherical nanoparticles, extract the potential along the dimer axis, and then use it in the quantum transport calculations⁶². The known defect of the LDA is that it misses the long-range correlations and fails to reproduce the image potential tail of the electron surface interactions¹⁰⁷. In Fig. 2 we show the potential obtained at the vacuum junction between Au surfaces for different separation distances. We compare the potentials obtained including the long-range image-charge interactions and using the DFT LDA calculations. The latter choice leads to overestimate significantly the barrier between the two surfaces⁶⁰. The QCM calculations presented in this paper use the potential model given by eqns. (1)–(4) that account for the image-charge interaction. The results in Fig. 2, which were obtained for a relatively simple static case of flat interfaces, represent all the information that will ultimately be required to implement the QCM, as we discuss in the next subsections. The probability of transmission through the junction for an electron moving perpendicular to the interface $T(\Omega, \ell)$ is determined by the potentials described here, and calculated as the ratio between the transmitted and incident electron fluxes across the gap.

2.2 Conductivity of the gap

It is possible to convert the calculated electron transfer probability $T(\Omega, \ell)$ into a static conductivity σ_0 of the plasmonic gap. Within a standard approach used in the description of e.g. STM junctions¹⁰⁶, the tunneling current density $J(V, \ell)$

through the junction between two planar jellium surfaces for a (small) applied bias V is given by¹⁰⁸:

$$J(V, \ell, \theta) = \frac{k_B \theta}{2\pi^2} \int_0^\infty d\Omega T(\Omega, \ell) \ln \left(\frac{1 + e^{(E_F + V/2 - \Omega)/k_B \theta}}{1 + e^{(E_F - V/2 - \Omega)/k_B \theta}} \right) \quad (5)$$

$T(\Omega, \ell)$ depends on the electron energy Ω and separation distance ℓ . The zero energy is placed at the bottom of the conduction band. The logarithmic factor accounts for the temperature θ effects arising from the Fermi-Dirac energy statistics in the leads, where k_B is the Boltzmann constant.

The conductance per unit area is given by:

$$G(\ell, \theta) = \left(\frac{\partial J}{\partial V} \right) \Big|_{V=0}, \quad (6)$$

where from eqn (5) one obtains the final expression for the conductance $G(\ell, \theta)$:

$$G(\ell, \theta) = \frac{1}{2\pi^2} \int_0^\infty d\Omega T(\Omega, \ell) \frac{1}{1 + e^{(\Omega - E_F)/k_B \theta}}, \quad (7)$$

We discuss the effect of temperature θ in subsection 5.1. We assume otherwise $\theta = 0$ K in the following and eqn (7) simplifies to

$$G(\ell) = \frac{1}{2\pi^2} \int_0^{E_F} T(\Omega, \ell) d\Omega. \quad (8)$$

Finally, assuming that the bias is given by $V = E\ell$, where E is the electric field in the vacuum gap between the metal surfaces, the conductivity of the junction $\sigma_0(\theta, \ell) = \frac{\partial J}{\partial E}$ is given by

$$\sigma_0(\ell) = \ell G(\ell), \quad (9)$$

which holds only for ℓ not too small. For very narrow gaps the described approach is not valid primarily because the fields in the junction can no longer be considered as homogeneous, so that the $V = E\ell$ approximation breaks.

Fig. 3 shows the electron transmission probability $T(E_F, \ell)$ between left and right leads, as calculated at the electron Fermi energy E_F for the Au junction. These results are obtained both with the model potential that accounts for the long-range interactions [given by eqn. (3) and eqn. (4)] as well as with the DFT LDA potential that misses the long-range contribution (potentials displayed in Fig. 2). Except for very narrow gaps $\ell \lesssim 2$ Å, $T(\ell)$ shows in both cases a nearly exponential dependence with the junction size ℓ , as typical of many tunneling processes. For small ℓ the potential barrier becomes low and the electrons are transferred from metal to metal via direct transitions over the barrier. The transmission probabilities tend then to 1 in a non-exponential manner as the gap closes, reflecting the formation of a continuous solid. Fig. 3 also demonstrates that, consistent with the overestimation of the potential barrier, the DFT LDA description results in too small transmission probabilities. The junction width where the tunneling process becomes important is underestimated by about 1 Å within DFT LDA.

Fig. 3 also shows that, similarly to the transmission probability $T(E_F, \ell)$, the static conductivity σ_0 (open circles) approximately follows an exponential

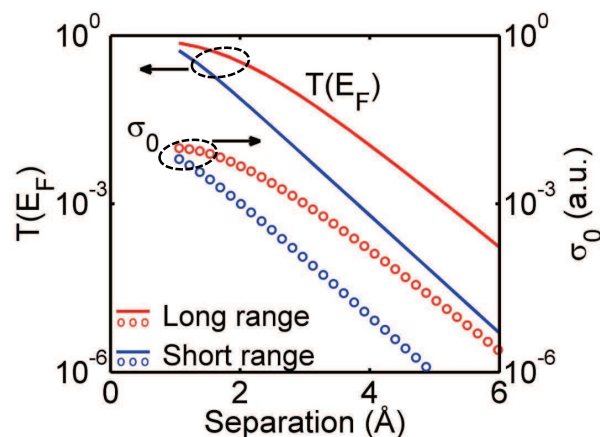


Fig. 3 Quantum-mechanical input to the QCM. Transmission at the Fermi Energy $T(E_F, \ell)$ (continuous line) and static conductivity σ_0 (open circles), both calculated quantum-mechanically, as a function of separation distance ℓ . The results are obtained for gold surfaces separated by vacuum when considering long range interactions in the potentials given by image charges [eqn. (3) and eqn. (4)] (red lines) and without considering these long range interactions within the DFT LDA (blue lines).

dependence with ℓ except for the shortest distances. Indeed, because of the rapid decrease of the transmission probability with lowering of the electron energy, only a small energy region around the Fermi level contributes to the tunneling current (conductivity σ_0) which is determined by $T(E_F, \ell)$ [see eqns. (8) and (9)]. The decay lengths of these two exponential functions are of the order of one atomic unit (\approx half \AA). The long range image-charge interactions also influence σ_0 considerably, as manifested by the faster decay of the conductivity with ℓ obtained using the LDA approximation (higher potential barrier in Fig. 2, blue lines) as compared to the more accurate model that includes the image potential (red lines).

2.3 Effective medium within the QCM: Drude metals in vacuum

We describe now how to account for the tunneling between plasmonic nanoparticles within the framework of classical Maxwell's equations which is the essence of the QCM. The interest in such approach is obvious since standard electromagnetic solvers can be applied so that the impact of quantum effects on the optical properties of practical plasmonic systems can be efficiently calculated. To some extent, the underlying idea here is similar to the text book examples relating e.g. the macroscopic dielectric constant of the medium to the polarizability of individual molecules¹⁰⁹. In this subsection, we concentrate on particles made of a free-electron metal and surrounded by vacuum.

The typical curvature radius R of plasmonic nanoparticles is of some tens of nanometers, much smaller than the gap widths at which tunneling effects become important. Under this condition, the quantum effects for a region of the nanogap characterized by a local separation distance ℓ can be modeled by assuming that

quantum effects in that position show similar behaviour to a pair of planar metal surfaces separated by the same separation ℓ . According to the discussion introduced in the previous sections, in the static case the current density between these two surfaces is given by

$$J(\ell) = \sigma_0(\ell)E. \quad (10)$$

Eqn. (10) describes the tunneling regime typical for STM with small and exponentially decaying σ_0 and an static homogeneous electric field E inside the junction. For time varying fields we use the adiabatic assumption that has proven its validity for example in the description of strong field ionisation in atomic and molecular physics^{100–102}. Under this assumption, the frequency-dependant currents and fields at the gap can be related through the static conductivity as

$$J(\ell, \omega) = \sigma_0(\ell)E(\omega), \quad (11)$$

where, similar to eqn. (10) homogeneity of the optical fields in the junction is assumed. Note that σ_0 is a *real* number so that the junction has resistive character. Similar equations have been recently derived^{110,111} within a framework of the Tien-Gordon theory developed for microwave fields¹¹². Our approach is valid for moderate separations of a few Å but not for ultra narrow gaps of atomistic dimensions, as the model does not account for field penetration into the nanoobject neither it allows for a simple interpolation of the tunneling and contact regimes.

Since the typical sizes of the tunneling gaps are at the nanometer scale, i.e., 100 times smaller than the wavelength of optical frequencies, eqn.(11) can be generally considered as a local one. One can now consider the relationship between the permittivity of an effective medium that fills in the gap of two plasmonic nanoparticles and the conductivity across the gap within *classical* Maxwell's equations:

$$\epsilon_g(\ell) = 1 + i 4\pi\sigma_0(\ell)/\omega, \quad (12)$$

and realize that this relationship connects classically the current density across the gap and the optical field inside the gap, exactly in the same way as the *quantum* relationship between the tunneling current and the field in the gap. We note that at this stage any description of the dielectric properties of the metal can be adopted (Drude, empirical,...), and $\sigma_0(\ell)$ can be calculated with quantum methods, as discussed earlier or with any other level of sophistication in the description of the junction.

While the simple model resulting in eqn. (12) describes the STM or tunneling regime with well separated nanoparticles, it does not allow to directly address all gap sizes down to the touching regime, where the junction progressively behaves as a continuous metal bridge. We seek an effective dielectric medium that has the permittivity described by eqn. (12) for large separations and that becomes identical to the surrounding metal at small ℓ . In this respect, assuming particles made of a free-electron Drude metal is instructive as it allows to obtain simple analytical expressions. Within the Drude model, the frequency-dependent permittivity of the particles is given by:

$$\epsilon_m(\omega) = 1 - \frac{\omega_p^2}{\omega(\omega + i\gamma_p)} \quad (13)$$

where ω_p is the plasmon frequency and γ_p describes the damping. In this paper we use $\omega_p = 9.065$ eV and $\gamma_p = 0.0708$ eV for gold, as extracted from a fit to empirical data at low energies¹¹³.

To describe the effective material at the gap, and taking into account that for small separations electrons are easily transferred and the gap becomes metallic, we also use a Drude-type expression, which allows an easy interpolation to the continuous metal case at $\ell = 0$. We write the permittivity ϵ_g of the effective medium at the gap as:

$$\epsilon_g(\omega, \ell) = 1 - \frac{\omega_p^2}{\omega(\omega + i\gamma_g(\ell))}, \quad (14)$$

which is related to the conductivity by

$$\sigma(\omega, \ell) = -i\omega(\epsilon_g(\omega, \ell) - 1)/4\pi. \quad (15)$$

The separation-dependent loss parameter γ_g allows to set the permittivity (and thus the conductivity) to a desired value for each ℓ . If we now require that the tunneling regime, given by eqn. (12), must be reproduced by eqn. (14) for large separation distances, $\ell \rightarrow \infty$, we obtain

$$\gamma_g(\ell) = \frac{\omega_p^2}{4\pi\sigma_0(\ell)}, \quad (16)$$

where we have approximated $\gamma_g(\ell) - i\omega \approx \gamma_g(\ell)$, since $\sigma_0(\ell)$ becomes exponentially small when ℓ increases (Fig. 3). Notice that within this approximation, due to the exponential increase of γ_g for large ℓ , eqn. (12) is recovered independently of the gap plasmon frequency assumed in eqn. (14). We take it as equal to the value describing the particles ω_p to facilitate recovering the metal permittivity ϵ_m when contact is established. In principle, one could directly apply eqn. (16) for each sufficiently large value of ℓ . Nonetheless, looking at the behaviour of σ_0 in Fig. 3 suggests using a simple exponential function.

For vanishing gaps the permittivity of the effective medium ϵ_g should tend towards the permittivity of the metals ϵ_m for all wavelengths, as the potential barrier between the particles disappears. Thus, for $\ell \rightarrow 0$ we should recover the dielectric constant of the Drude metal, or equivalently $\gamma_g \rightarrow \gamma_p$. However, eqn. (16) does not necessarily extrapolate directly to γ_p at $\ell = 0$ (due to the limitations on the quantum calculation of the conductivity σ_0 for small separations). We then proceed as follows. Taking into account the exponential dependence of σ_0 with separation found for moderate ℓ and the $\ell = 0$ limit, we impose

$$\gamma_g(\ell) = \gamma_p e^{\ell/\ell_c}. \quad (17)$$

The description of the effective material given by this simple exponential expression is a key aspect of the implementation of the QCM. ℓ_c is chosen to verify eqn. (16) for sufficiently large ℓ . In our implementation, we impose that eqn. (16) is exactly verified for the specific $\ell = \ell_0$ at which the transmission at the Fermi energy $T(E_F, \ell_0)$ is one percent. We explicitly checked that the final results are robust with respect to the choice of the matching point ℓ_0 , as far as it is located in the deep tunneling regime⁶². Fig. 4 shows the results for γ_g obtained for Au

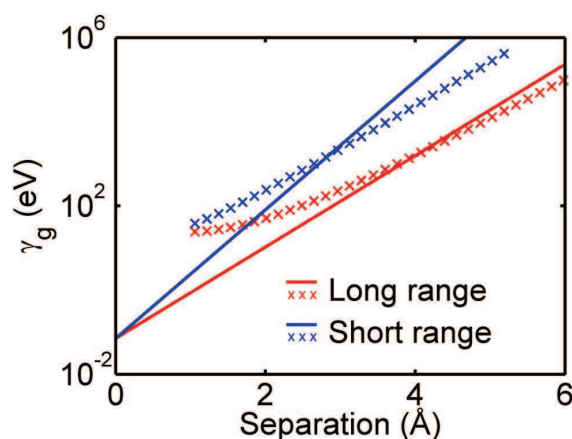


Fig. 4 Description of the effective medium used in the QCM. The loss parameter γ_g required for the effective medium in the gap is plotted as a function of separation distance ℓ . Solid lines correspond to the exponential expression used for the QCM implementation, while crosses are obtained from eqn. (16) using the static conductivity σ_0 calculated quantum-mechanically. The results are obtained for gold surfaces separated by vacuum with [red lines, Eqn. (3) and Eqn. (4)] and without [blue lines, DFT LDA] taking into account long-range image-charge interactions.

($\omega_p = 9.065$ eV, $\gamma_p = 0.0708$ eV), where we consider in the quantum calculation of σ_0 long range interactions [eqn. (3), red lines] or only short range interactions within the DFT-LDA approach are considered [eqn. (4), blue lines], as explained in previous sections. In the tunneling regime for $\ell \gtrsim 3$ \text{\AA}, the exponential dependence given by eqn. (17) provides a reasonable approximation to the $\gamma_g(\ell)$, obtained directly from the calculated tunneling characteristics using eqn. (16), particularly when the image charge interactions (long range) are accounted for. We obtain in this case $\ell_c = 0.4$ \text{\AA}. The discrepancy between eqn. (16) and the exponential fit becomes rather large at short distances, where the STM-type model resulting in eqn. (16) does not apply.

Following our procedure, γ_g becomes very large for large separation distances, obtaining resistive contacts, i.e., the effective material has mostly real conductivity. Indeed, at optical frequencies for sufficiently large separation distances, $\gamma_g(\ell) \gg \omega$, and the purely static conductivity is recovered $\sigma(\omega, \ell) = \sigma_0(\ell)$. As the gap closes γ_g decreases, $\sigma(\omega, \ell)$ becomes complex and the effective material acquires inductive character to become pure metallic at very small ℓ , recovering the value of the metal ϵ_m at both sides of the gap. The resistive to inductive transition is not described within tunneling STM theory, thus a direct comparison between predictions of the QCM and full quantum calculations is then needed in order to validate our approach.

We performed such an analysis for a Na nanosphere dimer. Na is a prototype of a free-electron metal with $\omega_p = 5.16$ eV, and $\gamma_p = 0.218$ eV. The JM approximation can then be used, allowing to perform full quantum Time-Dependent Density Functional Theory (TDDFT) calculations of the plasmonic response of a

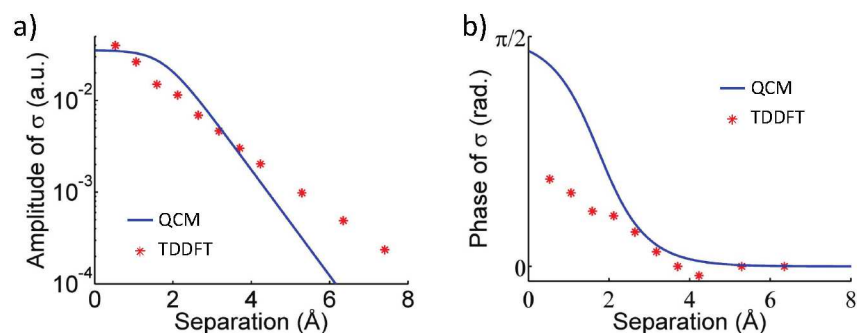


Fig. 5 Conductivity of the junction between two spherical Na nanoparticles. Results are shown as function of the width of the junction ℓ . (a) Amplitude and (b) phase of the conductivity, as given by TDDFT calculations (red stars) and as calculated with QCM (blue solid lines). The frequency corresponds to an energy of ~ 2.2 eV.

spherical nanoparticle dimer comprising 2148 electrons^{34,62}. Each Na sphere has a closed shell structure with 1074 electrons so that the nanoparticle response exhibits a well developed plasmon resonance. The sphere radius is $R_{cl} = 2.17$ nm. This is small compared with those in typical plasmonic experiments, but treating the correlations between the 2148 electrons contained in the dimer is already extremely heavy computationally. Fig. 5(a) and Fig. 5 (b) display the amplitude and phase of the gap conductivity σ as obtained within the QCM (effective medium from eqn. (15), blue lines) and from TDDFT calculations (red stars), for varying separation distance ℓ under excitation of radiation with energy $\hbar\omega \approx 2.2$ eV, close to the bonding dimer plasmon. In TDDFT, the conductivity is defined as the ratio between the current and the electric field at the central point between the nanoparticles.

For sufficiently large ℓ , both approaches give nearly real conductivity σ , manifesting the resistive nature of the contact and the validity of the adiabatic approach, according to which the tunneling current should have the same phase than the optical field due to the instantaneous response. As the distance decreases, the junction acquires inductive character, with a dephasing between the currents and the fields. The difference between the TDDFT and QCM data for the phase of σ is only significant at very narrow gaps, where the TDDFT gives larger efficient losses, probably linked with the finite cross-section of the junction, resulting in smaller phase. The agreement between QCM and TDDFT is also good for the module of the conductivity, with a somewhat larger disagreement for $\ell \gtrsim 6$ Å. In this regime, where $\ell \gtrsim R_{cl}$ for the small dimer considered in Fig. 5, the description of the junction as a composition of contacts between planar surfaces obviously breaks. However, we expect that the agreement will improve for common systems with larger R_{cl} . We also note that the tunneling is sufficiently small for $\ell \gtrsim 6$ Å so that it does not affect the optical response. In general, the agreement between the two approaches is surprisingly good, in particular considering the small radius of curvature of the plasmonic dimer considered for this comparison.

2.4 Generalization of the QCM to noble metals and dielectric gaps

In the previous section, we described the plasmonic material as a free-electron gas using the classical Drude permittivity given by eqn (13). This description is valid for materials such as Na but for noble metals such as gold or silver it does not account for the significant contribution of d -electrons to the optical response. Further, the surrounding medium was considered to be vacuum. The QCM can be straightforwardly extended to the case of arbitrary metals surrounded by any dielectric medium⁴⁶. The permittivity of metals ϵ_m , as obtained from the literature¹¹³, can be decomposed as:

$$\epsilon_m(\omega) = \epsilon_m^d(\omega) - \frac{\omega_p^2}{\omega(\omega + i\gamma_p)} \quad (18)$$

which explicitly distinguishes between the contribution from interband transitions involving d -electrons ϵ_m^d , and that from the free electron gas (right-hand side term). In contrast to eqn (13), ϵ_m^d does not need to be equal to 1 and can be frequency-dependent. ω_p and γ_p can be obtained from fitting ϵ_m at low frequencies, where the d -electron contribution is comparatively weak. For the calculations of gold dimers presented here $\omega_p = 9.065$ eV and $\gamma_p = 0.0708$. ϵ_m^d is then directly obtained from eqn. (18) using empirical data.¹¹³

To describe the permittivity of the QCM effective medium at the gap ϵ_g , we treat the free electrons as in the previous section and introduce a contribution of the d -electrons that decays exponentially for increasing gaps, with a decay length ℓ_d .

$$\epsilon_g(\omega, \ell) = \epsilon_0(\omega) + (\epsilon_m^d - \epsilon_0)e^{-\ell/\ell_d} - \frac{\omega_p^2}{\omega(\omega + i\gamma_g(\ell))}. \quad (19)$$

ϵ_0 is the relative permittivity of the surrounding dielectric medium, which does not need to be vacuum and can depend on frequency. $\gamma_g(\ell)$ in the Drude term is obtained as in the previous section [eqn (16) and eqn (17)], where we continue using the jellium approach to obtain the quantum value of the static conductivity σ_0 since the quantum charge transfer is dominated by the free electrons. A more complex ab initio calculations including the d -electrons and actual dielectric material in the plasmonic gap could also be used if feasible. ϵ_g thus tends to the permittivity of the particles for vanishing gaps, and to the value of the surrounding medium for large separations ($\gamma_g(\ell \rightarrow \infty) \rightarrow \infty$).

The decay length ℓ_d of the d -electron contribution $(\epsilon_m^d - \epsilon_0)e^{-\ell/\ell_d}$ is of the order of the Bohr radius since the electron density probability associated with the d -electrons is confined to the proximity of the metal. The exact value of ℓ_d can be set in several ways. For example, from the radial decay of the 5-d orbital¹¹⁴ we can set $\ell_d = 1.5$ a.u. ≈ 0.8 Å for gold and other typical materials. This is the value used in the calculations in this paper. We could also consider that the d -electron contribution should decay faster than the free-electron component, due to the higher localisation of the d -orbitals, and use a ℓ_d somewhat smaller than ℓ_c . Nonetheless, it is the Drude term that gives the critical conductive contribution to the permittivity setting the regime of conductive coupling between the nanoparticles across the gap. Therefore, as we have explicitly checked for local QCM calculations of Au dimers, the calculated optical response of the nanoparticle assembly is robust with respect to the specific choice of the ℓ_d .

2.5 Implementation of the QCM in classical Electrodynamics

We describe in this section how to implement the QCM using an electrodynamic solver of Maxwell's equations. The metallic particles are characterized as a medium of permittivity ϵ_m (possibly obtained from empirical data) that is delimited by sharp interfaces. The position of the interface is chosen at the jellium edge in the JM description of metal, as indicated in Table 1. This choice is not unique, and one can also consider the classical metal boundary defined by the position of the centroid of the screening charge at the surface^{86,87}. For the implementation of the QCM, however, it is important that the classical definition of ℓ corresponds to the one used in the quantum calculations of the tunneling current. This definition will be also relevant when comparing experiments and calculations with the aim of establishing a criterion of absolute separation distances.

The distance-dependent effective medium of permittivity ϵ_g described in the previous section needs to be inserted in the gap. In the general case of the nanoparticle dimer the junction is not between two planar surfaces so that there is not a single global distance. For each pair of opposite points separated by the local distance ℓ , the local ϵ_g can be set to the same value as the permittivity calculated for the corresponding ℓ -wide flat gaps. This simple approach assumes that the nanoparticle surfaces are of sufficiently large radius of curvature to be considered as locally flat, an assumption that should be valid considering typical experimental geometries. ϵ_g remains constant along the line joining opposite points, but can change as we move in the orthogonal direction of the gap, leading in general to an spatially inhomogeneous ϵ_g .

A general prescription to determine how to define opposite points and the connecting line is not necessarily straightforward, but typical structures often present a 'natural' option. For example, for configurations azimuthally symmetric with respect to a given axis [z in Fig. 1(a) and Fig. 1()], we define the local ℓ as the distance between opposite points linked by a line parallel to this axis. Conveniently, the expected polarization of the fields, which is critical for the tunneling, is also often expected to be along the same axis. For a more complex configuration it may be beneficial to define opposite points as those connected by a line parallel to the local electric field vector, and the distance as the length of this line.

Fig. 1(a) sketches the insertion in the gap of the effective medium with spatially-inhomogeneous permittivity ϵ_g , for a dimer composed of two metallic spheres. The plasmonic response can then be found using a classical solver of Maxwell's equations. For the results obtained here, two different solvers have been used: a finite element solver (COMSOL Multiphysics) and a boundary element method (BEM).¹¹⁵ The BEM requires the gap to be divided into different areas characterized by a mean distance to avoid inhomogeneous distributions of material. A possible implementation for the case of a bowtie antenna is sketched in Fig. 1(b). For azimuthally symmetric configurations, we have often found sufficient to consider $\sim 3 - 8$ shells placed in the region of the gap where the local distance is smaller than around 6 Å, but different scenarios may require different number of shells. For example, if field discontinuities are present at the contact regions between two shells and one of the particles, it can be convenient to use more shells.

The described implementation of the QCM comprises a series of steps to define the permittivity ϵ_g of the effective medium to be inserted in the gap. It is, however, possible to conceive modifications of the given procedure that would change to some extent the value of ϵ_g . In a previous work considering free-electron metals⁶², we showed very little change of the plasmonic response after modification of the exact definition. We have also verified that ignoring the contribution of the *d*-electrons to ϵ_g for two Au spheres does not essentially modify the extinction and near field enhancement spectrum within the local QCM model.

Thus, the QCM seems generally robust to modifications on the implementation details. Nonetheless, two conditions should likely be respected: the effective medium should have a strong resistive component except possibly for very narrow gaps, and ϵ_g should model correctly the exponential decay of the absolute value of the gap impedance with distance determined from the quantum calculations of the transmission probability.

3 Extension of the QCM to include nonlocal effects

A critical parameter for classical calculations is the relationship between the polarization induced in a material and the electric fields. Up to here, we have considered a local description of a metal. It assumes that the polarization at a point is proportional to the local fields at this same position, which introduces a certain error by ignoring the influence of the surrounding charge distribution, in particular for strong interaction between interfaces. This is precisely the case of small metallic particles and/or very narrow gaps.

Possibly the most common approach to introduce nonlocality when studying plasmonic systems within a classical framework is the hydrodynamical model^{116,117}, which considers an extra term in the dynamics of the free electron gas connected with its pressure and thus the deformation to an external perturbation. In this model, nonlocality is introduced in *k*-space by using a permittivity that is not only a function of frequency, but also of the wavevector *k*. In real space, this description corresponds to introducing an additional contribution to the polarization from the immediate vicinity of the non-uniform charge density, so that the polarization at each point is obtained via an integral comprising the electric fields over the surrounding region.

We have recently discussed how, for a pure free electron gas such as Na, the hydrodynamical model does not correctly reproduce certain aspects of the charge densities associated to the localized surface plasmons⁸⁷. The model predicts an electron density that decays considerably before the jellium edge defining the limit of the particles, i.e., the centroid of charge is displaced towards the interior within this approach. In contrast, full quantum simulations reveal that, for these free electron metals, the electron density is pushed a short distance towards the outside of the particles, i.e. there is a spill-out of the electrons. Nonetheless, for typical noble metals used in plasmonic experiments, the centroid of the charge is indeed displaced towards the interior of the particles due to the influence of the bound *d*-electrons, and the hydrodynamic approach can then be applied for practical purposes⁴⁷.

In the following, we describe briefly how we introduce the hydrodynamical approach into both the classical local and QCM theoretical frameworks. First we

discuss how the nonlocality is implemented into the optical response. Again, we consider separately the contribution from bound and free electrons, and write the electric displacement vector \vec{D} as:

$$\vec{D} = \vec{E} + 4\pi\vec{P}_d + 4\pi\vec{P}_c \quad (20)$$

with \vec{P}_d and \vec{P}_c the polarization vector for bound (d-electrons) and conduction electrons, respectively, and electric field vector \vec{E} . As in standard studies of the optical response of metal nanostructures, \vec{P}_d is described via a local approximation:

$$4\pi\vec{P}_d(\omega) = \epsilon_m^d(\omega)\vec{E}(\omega) \quad (21)$$

whereas nonlocal effects are incorporated by means of the polarization field \vec{P}_c . This free-electron polarization field is directly related to the induced current density $\vec{J}_c = \partial\vec{P}_c/\partial t$. For the implementation of nonlocal effects into the COMSOL Multiphysics package it is much more convenient to work with \vec{J}_c instead of \vec{P}_c . In the hydrodynamical model, the time evolution of the induced current density due to conduction electrons is described by the linearized Navier-Stokes equation:

$$\frac{\partial\vec{J}_c}{\partial t} + \gamma_p\vec{J}_c = \frac{\omega_p^2}{4\pi}\vec{E} - \beta^2\vec{\nabla}n \quad (22)$$

where $n = -\vec{\nabla}\vec{P}_c$ is the induced charge density. One immediately recognizes the nonlocal contribution from the free electrons, i.e., the dependence on the gradient of the induced charge density. Typically $\beta = \sqrt{3/5}v_F$, where v_F is the Fermi velocity. In particular, one can show that in the frequency domain:

$$\beta^2\vec{\nabla}(\vec{\nabla}\vec{J}_c) + \omega(\omega + i\gamma_p)\vec{J}_c = i\omega\frac{\omega_p^2}{4\pi}\vec{E}. \quad (23)$$

This equation for the induced current density and Maxwell's equations are coupled through their mutual dependence on the electric field \vec{E} and \vec{J}_c . They can be solved simultaneously in COMSOL by choosing appropriate boundary conditions for \vec{J}_c , such as continuity of its normal component. This implementation of nonlocal effects into our numerical framework reduces to a local response when β is simply set to zero, making the integration of a local and nonlocal description of different parts of a plasmonic system easy to realize.

Inclusion of the effective gap material in the hydrodynamical model leads to what we named before as nonlocal QCM. An equation similar to eqn (23) can be written within the gap region:

$$\beta^2\vec{\nabla}(\vec{\nabla}\vec{J}_c) + \omega(\omega + i\gamma_g)\vec{J}_c = i\omega\frac{\omega_p^2}{4\pi}\vec{E} \quad (24)$$

where γ_g (see section 2.3 for its definition) replaces γ_p . At the current stage, for the sake of simplicity, we assume that the optical response within the gap region is local, i.e., $\beta = 0$ in the region. Regarding the polarization contribution coming from bound electrons, it is treated in the same way as in local QCM and, therefore, it does not appear explicitly in eqn (24).

Complementary to the hydrodynamical model, we also consider a simple approach to nonlocality introduced previously^{86,87}, based on a simple rescaling of

the separation distances to take into account the spatial distribution of the electrons. To calculate the nonlocal results for two particles at a physical distances d , as defined by the jellium edges, it is simply required to obtain the classical local response at $d + d_n$ separation, where d_n is a distance given by the position of the two centroids of charge, $d_n = -1.8 \text{ \AA}$ for Na and $d_n \sim 1.7 - 3.0 \text{ \AA}$ for Au. This approach proved to be successful when predicting the observed peak positions for two Na wires and distances up to a few Ångströms⁸⁷. Unfortunately, it is not evident how to implement this method when a non-negligible quantum charge transfer between the particles is considered, and thus it is only used here for classical nonlocal calculations before contact. Other approaches to introduce nonlocality have been recently discussed, such as adding an extra dielectric layer of well defined properties to mimic the nonlocal displacement of the centroid of charge at the surface.⁸⁸

4 Nonlocality and quantum effects in the plasmonic response

In the following, we analyze the response of a plasmonic dimer as a function of separation distance to explore the different regimes sketched in Fig. 1(c): local, nonlocal, and quantum. We calculate the optical response of a dimer composed by two Au spheres of $R = 25\text{nm}$, using a local or nonlocal hydrodynamic description and with or without inclusion of the interparticle electron tunneling within the QCM. In all calculations we solve the classical electromagnetic Maxwell's equations to obtain the optical response of the system. However, to distinguish between different approaches, we denote as *classical local* the calculations where the optical response of the metal is described by a local dielectric constant without charge transfer across the gap, *classical nonlocal* refers to calculations where the metal response is described within the hydrodynamical approach, also without considering charge transfer between particles, the *QCM local* calculations use a local dielectric constant for the metal and include the electron tunneling within the QCM, and last, *QCM nonlocal* calculations consider the hydrodynamical approach for the metal response and the QCM to include charge transfer due to the tunneling.

The system holds cylindrical symmetry with respect to the z axis that connects the particle centers, located at $z_{\pm} = R \pm d/2$. d thus indicates the distance between the two closest points between the particles (different from the local separation ℓ) and z_{\pm} is measured from the center of the junction. $d < 0$ corresponds to overlapping particles. Experimental values of the gold permittivity are used¹¹³ and a plane-wave polarized along the dimer axis illuminates the system. The near-field enhancement $|E_g/E_0|$ is defined as the ratio between the electric field amplitude at the center of the gap E_g and the amplitude of the incident field E_0 . After contact, the fields inside the metallic junction are strongly screened therefore we only show the field enhancement for positive distances d . Non-local results are performed with the Finite Element Method (COMSOL Multiphysics), and the local calculations are obtained using the Boundary Element Method (BEM). We test that both methods provide the same results for the case of QCM local calculations.

The classical local response of dimers has been studied by many different groups and is generally well understood^{21,118,119}. We show the extinction spectra

and near-field enhancement at the gap of the Au dimer for several representative separation distances in Fig. 6(a) and Fig. 7(a), respectively. As pointed out above, the near-field spectra are shown only for positive separation distances as the local field gets quenched for overlapping dimers. As the spheres approach, the Coulomb interaction leads to strong charge concentration at the opposed metal surfaces, and thus to very intense fields¹²⁰ in the gap and to hybridized plasmonic modes that redshift strongly. The charges are antisymmetric with respect to the plane perpendicular to the axis of the dimer at the center of the gap ($z = 0$). Dark symmetric modes are not excited in our planewave scheme of illumination. For moderate separations d , the lowest-energy Bonding Dimer Plasmon (BDP) dominates the response, but for small d higher order modes are also efficiently excited. All modes have a clear signature in both the extinction and the near field. As the gap closes $d \rightarrow 0^+$, both the redshift of the modes and the magnitude of the associated field enhancement diverge.

The response changes abruptly when conductive contact is established at $d \leq 0$. For overlapping particles, electron transfer between the particles becomes possible, and the Charge Transfer Plasmon (CTP) modes^{29–31,121?} emerge. The lowest energy CTP appears at distinctively large wavelengths and corresponds to a dipolar-like oscillation characterized by non-zero net charges of opposite sign at each particle, an unphysical situation before contact. For small overlaps the narrow wedges support very fast spatial oscillations of the charge distribution¹²² leading to many high order modes. The resonant wavelength of these modes also diverges for $d \rightarrow 0^-$. As the overlap increases, the modes blueshift until eventually the spectra of a single sphere would be recovered.

The divergence of the results as $d \rightarrow 0$, right before and after contact, is related to the description of the sharp interfaces between the metal and the surrounding medium within the local classical approach. This leads to extremely large and confined charges at the sharp wedges and narrow gaps producing the divergence. Rounding the edges of the neck of the contact between two particles would considerably diminish the expected number of resonances, their redshift and the field enhancement. While Ref.²¹ discusses the implications of geometrical rounding, nonlocal and quantum tunneling effects also result in effective rounding of the geometry of the junction as follows from the results below. Accounting for the nonlocal response within the hydrodynamical approach allows to remove the unphysical divergences of the optical response of narrow gaps^{47,81} as shown in the results of Fig. 6(b) and Fig. 7(b).

Local and hydrodynamical nonlocal calculations indicate several similarities both in their far field [Fig. 6(a) and Fig. 6(b)] as well as in the near field response [Fig. 7(a) and Fig. 7(b)]. As the particles approach, the modes redshift strongly and the corresponding field enhancement increases. Particle contact results in an abrupt change in the spectra with the appearance of the Charge Transfer Plasmons that blue-shift with increasing overlap. However, important differences appear between the two models. Compared to the local results, the nonlocal description generally 'softens' the spectral trends⁸⁵, as it captures the lack of sharp interfaces in real systems. As distance goes to zero, either before or after contact, both the shifts of the modes and the number of resonances efficiently excited are smaller than for the local classical results. In a similar manner, the field enhancement predicted by the nonlocal approach can be very large just before contact but not

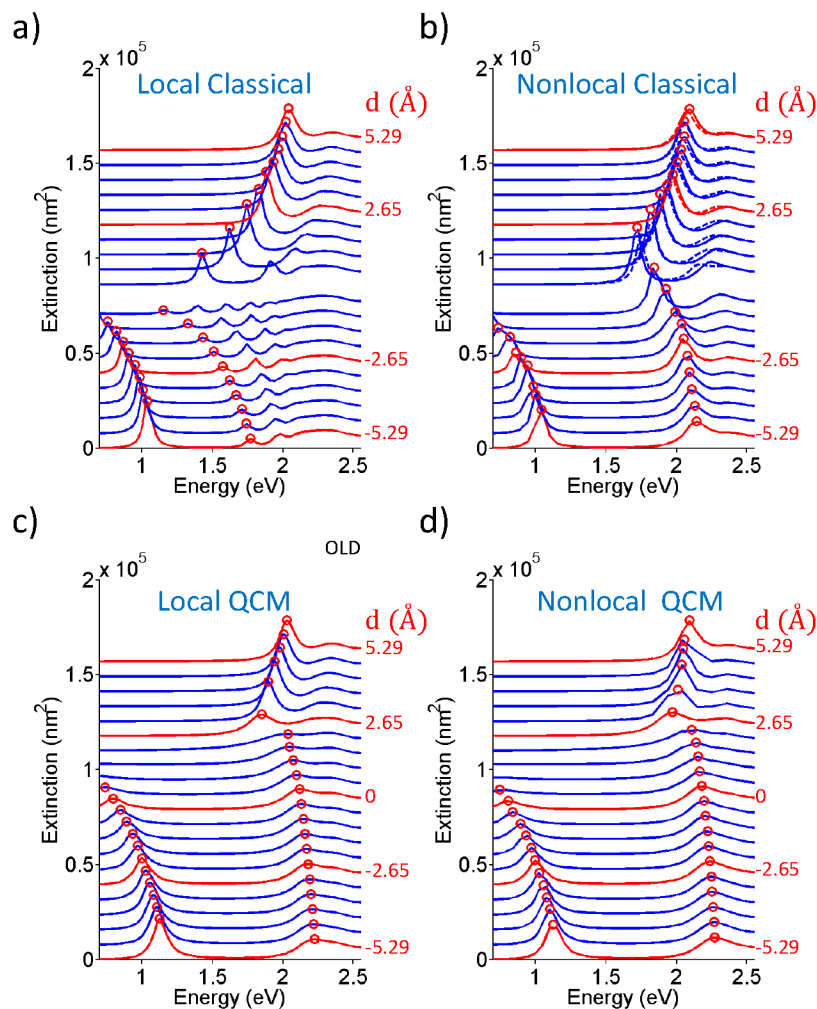


Fig. 6 Extinction cross-section of an Au dimer for different separation distances d within (a) the local classical model, (b) the nonlocal classical model, (c) the local QCM and (d) the nonlocal QCM. The solid lines in (b) correspond to the hydrodynamical model and the dashed lines for $d > 0$ to the values obtained after rescaling the results from local classical calculations by $d_n = 2 \text{ a.u.} = 1.06 \text{ \AA}$. The system is composed of a dimer of 25 nm radius Au spherical particles in vacuum, illuminated by a plane-wave polarized along the dimer axis. The results are plotted for d steps of 1 a.u. (0.529 \AA) and shifted vertically for clarity, with some representative distances indicated on the right. $d < 0$ correspond to overlapping particles. The classical local and nonlocal extinction spectra for $d = 0$ are not plotted as in the absence of tunneling, the geometry is ill defined when contact is just established. Red open circles indicate positions of the maxima of the modes that are further analyzed in Fig. 8.

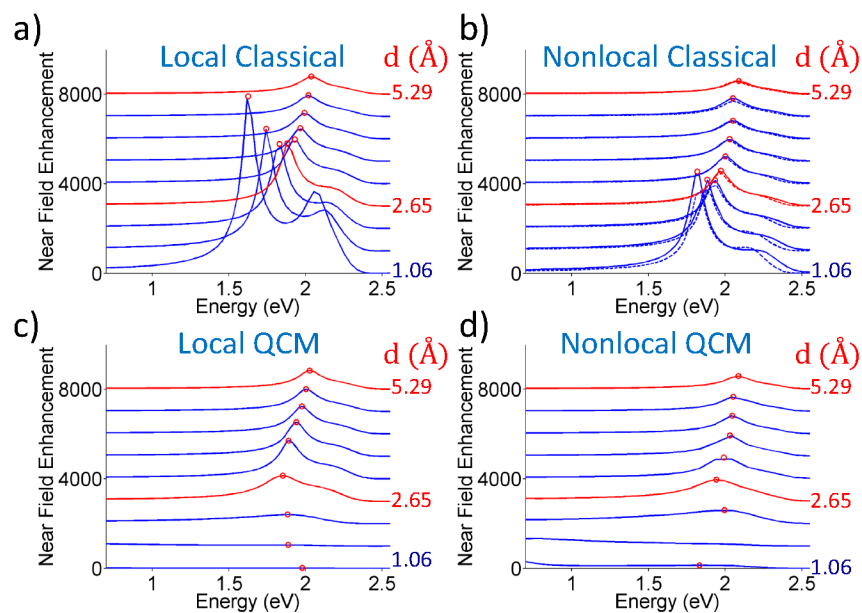


Fig. 7 Near field enhancement at the centre of the gap $|E_g/E_0|$ between two 25 nm radius Au spheres in vacuum as a function of separation distance d within (a) the local classical model, (b) the nonlocal classical model, (c) the local QCM and (d) the nonlocal QCM. The solid lines in (b) correspond to the hydrodynamical model and the dashed lines to the values obtained after rescaling the results from local classical calculations by $d_n = 2 \text{ a.u.} = 1.06 \text{ Å}$. The system is composed of a dimer of 25 nm radius Au spherical particles in vacuum, illuminated by a plane-wave polarized along the dimer axis. The results are plotted for d steps of 1 a.u. (0.529 Å) and shifted vertically for clarity, with some representative distances indicated on the right. Red open circles indicate the position of the maxima of the modes that are further analyzed in Fig. 8.

as large as obtained in the local case, with no apparent divergence as the gap closes. In general, the differences between the two models are more significant for narrow gaps or small overlaps. For example, when d changes from 2 to 1 a.u. (1.06 to 0.53 nm) the local classical calculations predict that the low-energy BDP extinction resonance peak redshifts from 765 nm to 871 nm, and that the near field enhancement increases from 8100 to 14400. This is to be compared with a wavelength change from 685 nm to 720 nm, and a field enhancement increase from 4600 to 7200, obtained within the nonlocal hydrodynamical model for the same separation distances.

The distribution of surface charges is critical to understand the differences between the local and non-local classical responses. While in the local classical calculations the plasmon-induced screening charges are located at the geometrical surfaces of the metal, using the nonlocal hydrodynamic model results in a displacement of the screening charges into the metal, inwards from the metal surface^{80,86,87,123,124}. Thus, when the distance between the geometrical surfaces is zero, the screening charges across the junction are separated by a distance d_n , where $d_n/2$ is the position of the centroid of the screening charge with respect to the geometrical surface (jellium edge) of the individual nanoparticles. Since the screened charges do not abruptly overlap when contact is established, the electrostatic interactions in the system do not diverge, in clear contrast to the classical model where infinite localization of the charges is produced. The effect of the spatial dispersion of the response is thus to round the sharp wedges of overlapping geometries⁸⁵.

The effect of the shift of the centroid of the screening charge with respect to the geometrical surfaces of the gap can be further explored for $d > 0$ by using the concept of distance rescaling⁸⁷. In Fig. 6(b) and Fig. 7(b) we show spectra corresponding to local classical calculations where the separation distance is rescaled to $d + d_n$ (with $d_n = 2$ a.u. = 1.06 Å) given by the actual separation distance given by the position of the screening charges, and not by the system geometry. Notably, this simple approach is in very good agreement with the more complex hydrodynamical calculations, which supports the interpretation that the main role of nonlocality is to displace and spread the centroid of charge density, effectively lifting unphysical divergences.

We move next to one of the main aspects of this discussion, the quantum effects due to electron tunneling across the junction, as captured using the QCM. Fig. 6(c) and Fig. 7(c) show the far- and near-field QCM results, respectively, for a local description of the plasmonic response. For $d \gtrsim 3.5$ Å, the tunneling starts being negligible and thus the classical behaviour is recovered. However, for shorter distances, as well as for all the overlapping cases considered, the electron tunneling strongly modifies the response, as expected from previous studies of related systems^{34,60,62}. We thus denote the region of separations $d < 3 - 4$ Å as the tunneling regime. Due to the tunneling current that emerges before contact and neutralizes the induced charges of opposite sign at the junction, the classical discontinuity of the optical response at contact, $d = 0$, is removed. In contrast, the QCM calculations of the extinction cross-section [Fig. 6(c)] show a gradual transition, with a threshold distance $d_{th} \approx 0.35$ nm separating two different situations^{34,60}. As the gap closes, still being larger than d_{th} , the hybridized plasmonic modes of the dimer redshift similar to the results of classical calculations. At

$d = d_{th}$ the redshifting modes gradually disappear and new modes corresponding to the Charge Transfer Plasmons (CTPs) emerge that blueshift with further decrease of d .^{33,125} The emergence of the CTPs at small but positive separation distances $d > 0$ points out that the conductive contact between nanoparticles is established prior to the direct geometrical overlap of their surfaces, owing to the electron tunneling through the potential barrier separating the nanoparticles.

The QCM extinction spectra exhibit a moderate number of modes for all separation distances, in contrast to the prediction from local classical calculations of dimers with narrow gaps and small overlaps. In the nonlocal classical case, we discussed the relatively small number of modes as a consequence of the gradual variation of the electron distribution near the interfaces, which softens the plasmonic response. In the QCM, the softening is due to the charge transfer across the separating vacuum. The transfer probability, as codified by ϵ_g , changes gradually as we move transversally (plane xy) away from the center, from basically metallic to identical to the surrounding vacuum.

The results of the local QCM also show how the charge transfer between particles at tunneling distances has a dramatic effect on the near field enhancement at the center of the gap. For sufficiently large gaps $d \gtrsim d_{th}$ the classical results are basically recovered, with increasing enhancement for narrowing gaps. However, for distances smaller than $d \approx d_{th}$, where the strongest enhancements are found, the quantum electron transfer screens the charges at the gap, quenching the near fields. This quenching can have important consequences in different optical techniques, such as surface-enhanced spectroscopies, where large field enhancements are often necessary.

Last, we analyze the situation where nonlocality and electron transfer across the gaps are included simultaneously in our QCM calculations with a hydrodynamical treatment of the metal response, as introduced in section 3. For sufficiently large separation distances above d_{th} the tunneling is negligible and the nonlocal screening is the main reason of the difference with classical local descriptions. We thus recover the classical nonlocal results both for the extinction, shown in Fig. 6(d), and for the near-field enhancement, Fig. 7(d). For separations below d_{th} , the nonlocality also modifies the details of the response, as observed when comparing the results of nonlocal QCM with those of the local QCM simulations. Nonetheless, the influence of nonlocality on the response remains relatively small when compared with the effect of quantum tunneling. The latter is thus the key aspect determining the optical response of the system. Generally, the nonlocal and local QCM calculations yield very similar results over the entire range of separations considered here.

Fig. 8(a) and Fig. 8(b) show the synthetic summary of the results obtained in this section using local classical, nonlocal classical, local QCM and nonlocal QCM calculations. The energy of the extinction plasmon resonance [Fig. 8(a)] and the resonance near-field enhancement [Fig. 8(b)] are shown as function of the distance between nanoparticles, d , for the most relevant plasmon modes. In particular, Fig. 8(a) shows the spectral position of the extinction peaks for the lowest energy BDP mode that exists for positive distances (down to $d \gtrsim d_{th}$ when using the QCM, and to $d > 0$ for the classical treatment) as well as for the two lowest energy CTP modes that emerge at $d \lesssim 1\text{\AA}$ within the QCM and from $d < 0$ for classical treatments. Fig. 8(b) focuses on the range of $d \geq 0$ and displays the

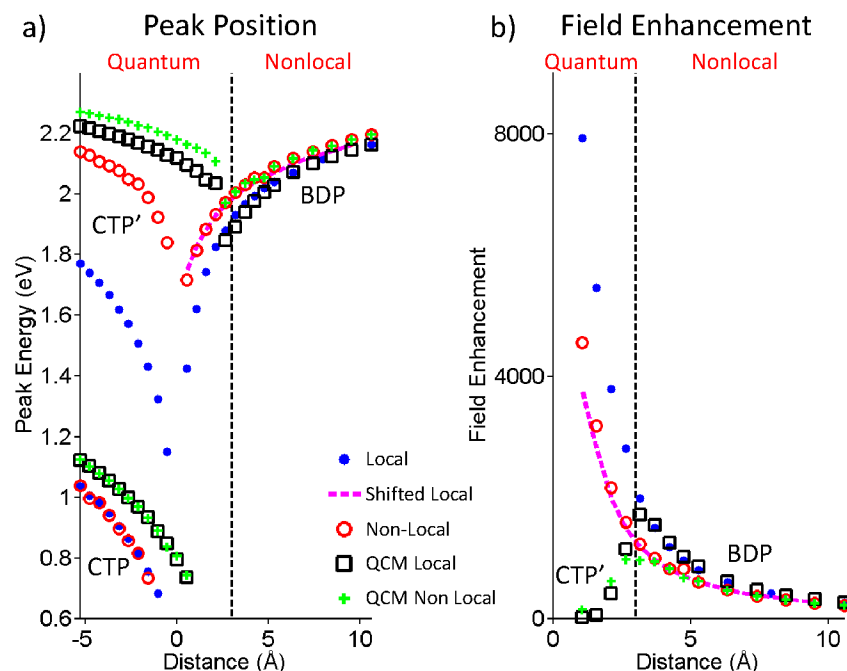


Fig. 8 Summary of the response predicted by the different models. (a) Wavelength of extinction peaks of the main plasmon modes, and (b) maximum near field enhancement $|E_g/E_0|$ at the center of the gap as a function of separation distance, for local classical (blue dot), nonlocal classical (red open circle for hydrodynamical model and magenta dashed line for distance rescaling), local QCM (black open square) and nonlocal QCM (green +, calculated with the hydrodynamical formalism). The values correspond to those indicated by circles in Fig. 6 and Fig. 7. The vertical dashed line corresponds to $d = 3.0$ Å and approximately separates the distance ranges where either the quantum-induced charge transfer or nonlocal effects dominate the response, as indicated at the top of the figure. The labels of the plasmon peaks refer to the Bonding Dimer Plasmon (BDP) and to the two lowest-energy Charge Transfer Plasmons (CTP and CTP').

maximum field enhancement of the BDP, as well as of the second CTP' charge transfer plasmon which emerges at ≈ 2.1 eV in the QCM calculations for $d \lesssim d_{th}$. The data points in Fig. 8(a) and Fig. 8(b) are extracted from Fig. 6 and Fig. 7, where they are marked with open circles. Along with the nonlocal results obtained within the hydrodynamical model, we also show the results obtained with the distance rescaling, where the nonlocal results at distance d are taken as equal to the local values at $d + d_n$. As already discussed, we obtain a good agreement with the hydrodynamical approach for $d_n = 1.06$ Å.

Considering the plasmonic response of the dimer, three regions of the interparticle separations d emerge, consistent with the introductory sketch of Fig. 1:

- At large separations (in our case for $d \gtrsim d_{cl} = 2$ nm (not shown in Fig. 8)) the local classical approach adequately captures the plasmonic response so that we identify this distance range as the *classical regime*.
- For $d_{th} \lesssim d \lesssim d_{cl}$ the differences between the local and nonlocal hydrodynamical results are clearly visible, and the electron tunneling through the potential barrier separating the nanoparticles is negligible. This is the *non-local regime*. According to the distance rescaling, including nonlocal effects gives a similar effect as modifying the distance in the local calculations by a factor $(1 + d_n/d)$, which allows to understand the increasing role of the nonlocality for narrowing gaps. Note that the d_n/d variation should relate to a *relative* change in the spectral response between nonlocal and local results. The *absolute* change would depend also on the size of the particles, so that for large structures nonlocal effects can remain significant for larger separations.
- The distance range $d < d_{th}$ corresponds to the *quantum regime*. At this Ångstrom-scale separations, the electron transfer across the junction dominates the optical response, and the differences between the nonlocal QCM and local QCM results remain relatively small. Nonlocality does modify to some extent the exact response, as can also be seen in Fig. 8. Nevertheless, the prediction of the local QCM calculations seems sufficient to understand most of the features of the plasmonic response.

To finish this section, we emphasize three particularly clear signatures of the tunneling regime for closely interacting spherical nanoparticles.^{60,62} (i) the gradual transition in the dispersion of the gap modes at a small threshold separation distance d_{th} , where the modes stop redshifting and start a progressive blueshift as the particles become closer, (ii) the emergence of a CTP mode at low energies already for (small) positive distances, and (iii) the quenching of the near fields. The presence of much fewer modes for small overlaps and narrow gaps when comparing local QCM with local classical calculations is also striking but may not be the easiest path to identify quantum effects, as the number of modes is also comparatively small for nonlocal classical calculations or, after contact, for local classical results with rounded wedges²¹. We also notice that the signature of quantum effects on the far-field signal depends on the morphology of the gaps¹²⁶. An additional consequence of quantum effects is that the significant quenching at the center of the gap expels the strong fields outside and thus establishes an intrinsic quantum limit to the ultimate field confinement^{6,46}.

5 Extension of the QCM to different materials and temperatures

We have focused up to now on gold dimers at 0K, but the QCM can be applied to more general materials and circumstances in plasmonics. We discuss in the following the effect of changing the temperature and of considering other metals.

5.1 Effect of Temperature

The quantum conductivity σ_0 used in the implementations of QCM discussed above has been obtained from eqn (8) assuming tunneling at 0K temperature. More generally, eqn (7) should be applied to calculate the conductivity for non-zero temperature.

Fig. 9(a) shows the static conductivity σ_0 of the vacuum gap between two flat Au surfaces. Results are obtained using eqn (7) as a function of the gap separation ℓ for the case of zero temperature (open red circles), 500K (open blue circles) and 5000K (open green circles). The temperature-independent electron transmission probability at the Fermi energy $T(E_F)$ is also shown for reference by the continuous line. The results are obtained as described in subsections 2.1 and 2.2. Fig. 9(b) plots the distance and temperature dependent loss parameter γ_g used in the QCM description of the effective medium. A continuous line shows the results of the exponential approximation given by eqn. (17), and symbols show the results for γ_g directly deduced from σ_0 using eqn. (16). The results for 0K are identical to those presented in Fig. 3 and in Fig. 4.

Most notably, σ_0 and γ_g , which parameterize the electron transfer due to quantum tunneling, are very little sensitive to the temperature. The results for 0K and 500K are essentially identical, with the difference small enough not to be appreciated in the figure. Even for a temperature as high as 5000K, which is considerably larger than the melting point of gold, the induced change of σ_0 and γ_g remains small. σ_0 is robust to temperature changes because the ensuing smearing of the Fermi distribution symmetrically opens the channels for the electron tunneling in both directions. While the electron energy dependence of the barrier transmission $T(\Omega)$ breaks this symmetry, the characteristic electron energy scale of the change of $T(\Omega)$ is a fraction of eV. This requires very high temperature for the corresponding electronic states to be populated. For practical purposes, the observed temperature dependence of γ_g should be negligible, inducing much weaker changes than other temperature-dependent effects such as thermal expansion of the nanoparticles or changes in the bulk permittivity of gold.

5.2 Other materials

The QCM can be applied to other metals besides Au in a straightforward manner, following the description in Sections 2 and 3. Fig. 9(c) shows the evolution with ℓ of the tunneling probability at the Fermi energy $T(E_F)$ and of the quantum-mechanically calculated static conductivity σ_0 , for Au, Ag, Cu and Na surfaces separated by vacuum. The results are generally similar in all these cases, particularly for the three noble metals. Overall, the lower is the metal work function (see Table 1 for the work functions of Na, Au, Ag and Cu) the larger is the conductivity and thus the smaller is the loss parameter for a fixed value of gap separation

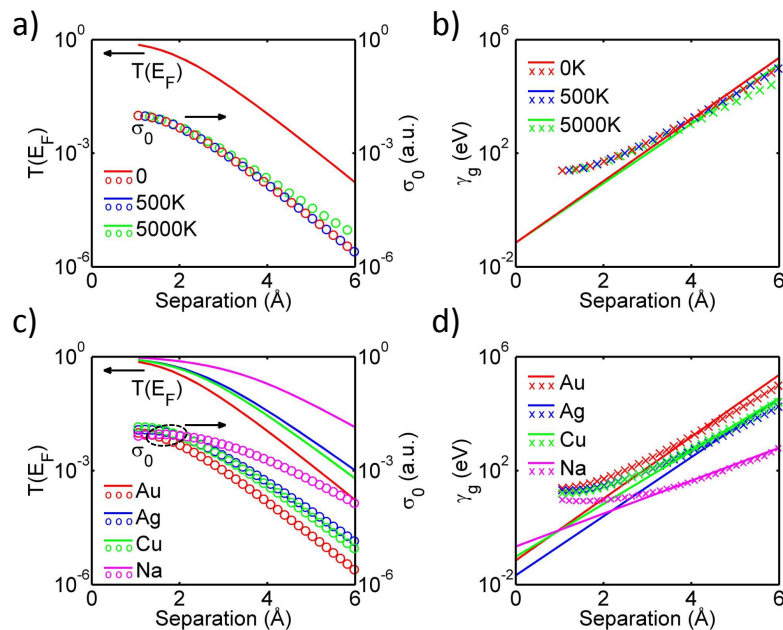


Fig. 9 Modeling for different materials and temperatures. (a, c) Tunneling probability at the Fermi Energy $T(E_F)$ (solid lines) and quasi-static conductance σ_0 (open circles) as a function of gap separation distance obtained from quantum-mechanical calculations. In (a) different temperatures are considered (0K in red, 500K in blue, and 5000K in green). $T(E_F)$ is independent of temperature therefore all three curves fall on the same position, and so do the red and blue circles of σ_0 . Values represented here for Au at 0K correspond to those in Fig. 3 and Fig. 4. In (c) different materials are considered (Au in red, Ag in blue, Cu in green, and Na in magenta). (b,d) Tunneling loss parameter γ_g describing the effective medium in the gap as a function of gap separation distance. Solid lines correspond to the exponential expression used for the QCM implementation, while crossed points are obtained from eqn. (16) using the static conductivity σ_0 calculated quantum-mechanically. In (b) the same temperatures as in (a) are considered and overlap of lines for 0K and 500 K is produced. In (d) different materials are considered as in (c).

[see Fig. 9(d)]. For the four materials, and excluding the narrowest gaps, $T(E_F)$ and σ_0 follow an approximately exponential variation with ℓ . The exponential expression for γ_g used in the QCM [eqn (17)] is a good fit to the values directly deduced from σ_0 using eqn. 16, with the exception of very short distances where this equation does not apply.

From a practical perspective, to set the permittivity ϵ_g of the effective medium at the gap, the QCM requires to know the permittivity of the metal surrounding the gap (ϵ_m)¹¹³, the values of ω_p and γ_p determining the free-electron contribution to ϵ_m , and the characteristic lengths describing the distance dependence of the free-electron (ℓ_c) and bound d -electron (ℓ_d) terms defining ϵ_g . ω_p and γ_p can be obtained on the basis of the ω dependence of ϵ_m at large wavelengths, and ℓ_c and σ_0 as discussed in section 2. The d -electron contribution to the permittivity, ϵ_m^d , at $\ell = 0$ can then be obtained by subtracting the free-electron contribution from ϵ_m . For reference, Table 2 indicates the values used in our calculations for ω_p , γ_p , ℓ_c and ℓ_d in the case of Au, Ag, Cu and Na, all surrounded by vacuum. For pure Drude-metals such as Na, the d -electron contribution is absent and ℓ_d is not necessary. Notably, the decay length ℓ_c takes similar values for the three noble metals, but is noticeably larger for Na. For systems separated by water or dielectrics⁵³, we also expect to find significantly larger ℓ_c .

	ω_p (eV)	γ_p (eV)	ℓ_c (Å)	ℓ_d (Å)
Ag	9.175	0.0212	0.42	0.79
Au	9.065	0.0708	0.4	0.79
Cu	8.853	0.0954	0.47	0.79
Na	5.16	0.218	0.75	-

Table 2 QCM parameters for Au, Cu, Ag and Na in vacuum: plasma frequency ω_p and losses γ_p of the Drude contribution to the dielectric function; characteristic length ℓ_c and ℓ_d of the exponential functions describing the increase of the loss parameter, and the decay of the d -electron contribution to the screening, respectively. ℓ_c and ℓ_d are given in Å, and γ_g and ω_p are given in eV. The value of ℓ_d is the one used in our calculations although other alternatives are possible (see text for discussion). ℓ_d is not given for Na because d -electrons do not play a role in the screening in this material.

In Fig. 10 we compare the spectra of extinction and near field enhancement $|E_g/E_0|$ at the center of the gap of Au, Ag and Cu spherical nanoparticle dimers in vacuum as a function of the separation d of the gap. The field is polarized along the dimer axis, and the radius of each of the two identical nanoparticles is $R = 25$ nm. The qualitative effect of tunneling is very similar for all three cases. As has been already discussed for Au, the extinction exhibits a gradual transition from large distances to the overlapping regime, and the CTP resonances emerge just before physical contact is established. The transition occurs around a threshold distance d_{th} of a few Ångströms which separates a range of redshifting (towards contact) and a range of blueshifting (progressive overlapping) of the plasmonic modes. The near field enhancement is maximized for all three materials for a gap separation of a few Ångstroms, near d_{th} , and it is quenched strongly for narrower gaps. d_{th} is similar for the three cases due to the similar values of ℓ_c obtained. Along with the qualitative similarities, the quantitative differences in the permittivity of different metals can strongly affect the details of the plasmonic

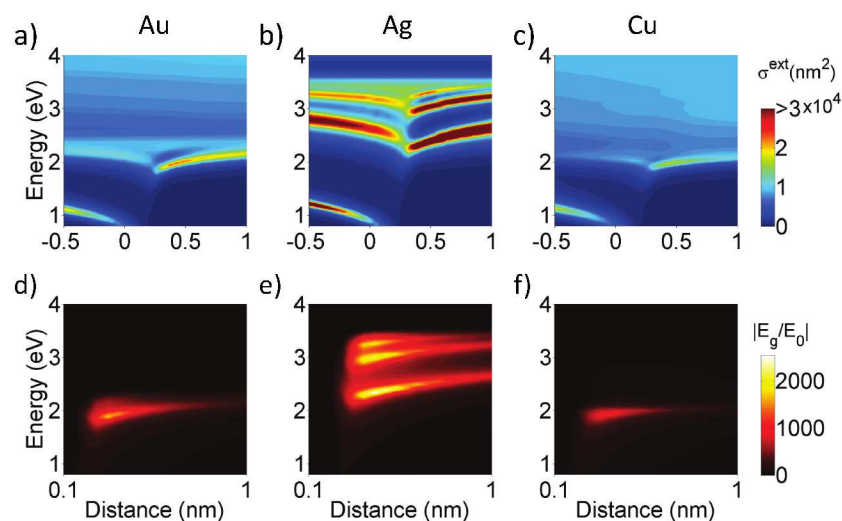


Fig. 10 Optical response for different materials. (a-c) Extinction cross-section σ^{ext} and (d-f) Near field enhancement at the gap center $|E_g/E_0|$ for (a,d) Au, (b,e) Ag and (c,f) Cu dimers, as a function of separation distance and energy. A radius $R = 25$ nm of the spherical particles and planewave illumination polarized along the dimer axis are used in all cases.

response. Indeed, the number, strength, and spectral position of the resonances show a significant material dependence, mostly due to the material dependence of the losses parameter γ_p and the d -electron contributions to the metal permittivity ϵ_m^d .

6 Discussion and Conclusions

In this paper, we have described in detail the Quantum Corrected Model, which allows accounting for the quantum tunneling with fully classical simulations of the optical properties of nanoparticle assemblies with narrow junctions. The main idea behind the QCM is to fill the interparticle junction with an effective material that results in the same local classical current density as the tunneling current density obtained from a quantum calculation. We describe the practical case of noble metals, which show a large contribution from d -electrons to the optical response. We provide a detailed description of the effective material for frequently used metals such as Au, Ag and Cu. We put particular emphasis in the extension of the QCM to incorporate the Hydrodynamical treatment of nonlocal effects, and discuss the effect of non-zero temperatures in the optical properties. While this paper focuses on the linear response, the QCM can be extended to non-linear phenomena^{34,127–129} by taking into account the dependence of tunneling across the gap on the strength of the local field.

We have also compared the respective influence of nonlocality and of quantum charge transfer on the plasmonic resonance of a dimer. Three regions of interparticle separations could be identified. Above a few nanometers, local clas-

sical calculations adequately describe the optical properties of plasmonic dimers. In the intermediate range of distances, above ≈ 0.35 nm, classical nonlocality modifies the exact properties of the plasmonic modes. Nonetheless, nonlocal effects do not change the qualitative behaviour predicted by classical local models and they can be modeled by simple distance rescaling. For junction widths below ≈ 0.35 nm the system is in the quantum tunneling regime. For these ultranarrow gaps, the charge transfer across the junction radically modifies the optical response of the dimer, leading to the quenching of the near fields and to a complete spectral redistribution of plasmonic modes. These strong effects cannot be captured even qualitatively by current classical theories based on the local or nonlocal hydrodynamic descriptions of the metal. The different relative influence of nonlocal and tunneling effects depending on separation distance should be observed in very general systems characterized by nanometer gaps, at least for spherical terminations¹²⁶, and can thus be helpful in the interpretation of experimental measurements.

Acknowledgements

RE and JA acknowledge financial support from project FIS2013-41184-P of MINECO and from project IT756-13 of consolidated groups of the Department of Education of the Basque Government. PZ and FJGV acknowledge financial support from the European Research Council (ERC-2011-AdG Proposal No. 290981, Plasmonoquanta). AGB and FJGV gratefully acknowledge the hospitality of Donostia International Physics Center. This work has been funded by part by the French Agence Nationale de la Recherche (ANR-2011-EMMA-003-01), and by Triangle de Physique.

References

- 1 K. L. Kelly, E. Coronado, L. L. Zhao and G. C. Schatz, *The Journal of Physical Chemistry B*, 2003, **107**, 668–677.
- 2 R. Alvarez-Puebla, L. M. Liz-Marzán and F. J. Garcá de Abajo, *The Journal of Physical Chemistry Letters*, 2010, **1**, 2428–2434.
- 3 J. A. Schuller, E. S. Barnard, W. Cai, Y. C. Jun, J. S. White and M. L. Brongersma, *Nature Materials*, 2010, **9**, 193–204.
- 4 N. J. Halas, S. Lal, W.-S. Chang, S. Link and P. Nordlander, *Chemical Reviews*, 2011, **111**, 3913–3961.
- 5 A. J. Pasquale, B. M. Reinhard and L. Dal Negro, *ACS Nano*, 2011, **5**, 6578–6585.
- 6 H. Cang, A. Labno, C. Lu, X. Yin, M. Liu, C. Gladden, Y. Liu and X. Zhang, *Nature*, 2011, **469**, 385–388.
- 7 H. Xu, E. J. Bjerneld, M. Käll and L. Börjesson, *Phys. Rev. Lett.*, 1999, **83**, 4357–4360.
- 8 C. E. Talley, J. B. Jackson, C. Oubre, N. K. Grady, C. W. Hollars, S. M. Lane, T. R. Huser, P. Nordlander and N. J. Halas, *Nano Letters*, 2005, **5**, 1569–1574.
- 9 J. Theiss, P. Pavaskar, P. M. Echternach, R. E. Muller and S. B. Cronin, *Nano Letters*, 2010, **10**, 2749–2754.
- 10 M. Moskovits, *Rev. Mod. Phys.*, 1985, **57**, 783–826.
- 11 B. Fazio, C. D'Andrea, F. Bonaccorso, A. Irrera, G. Calogero, C. Vasi, P. G. Gucciarci, M. Allegrini, A. Toma, D. Chiappe, C. Martella and F. Buatier de Mongeot, *ACS Nano*, 2011, **5**, 5945–5956.
- 12 P. Mühlischlegel, H.-J. Eisler, O. J. F. Martin, B. Hecht and D. W. Pohl, *Science*, 2005, **308**, 1607–1609.
- 13 P. Bharadwaj, B. Deutsch and L. Novotny, *Adv. Opt. Photon.*, 2009, **1**, 438–483.

- 14 T. H. Taminiou, F. D. Stefani, F. B. Segerink and N. F. Van Hulst, *Nature Photonics*, 2008, **2**, 234–237.
- 15 J. N. Farahani, H.-J. Eisler, D. W. Pohl, M. Pavius, P. Flückiger, P. Gasser and B. Hecht, *Nanotechnology*, 2007, **18**, 125506.
- 16 L. Rogobete, F. Kaminski, M. Agio and V. Sandoghdar, *Opt. Lett.*, 2007, **32**, 1623–1625.
- 17 R. Esteban, T. V. Teperik and J. J. Greffet, *Phys. Rev. Lett.*, 2010, **104**, 026802.
- 18 S. Kim, J. Jin, Y.-J. Kim, I.-Y. Park, Y. Kim and S.-W. Kim, *Nature*, 2008, **453**, 757–760.
- 19 A. García-Martín, D. R. Ward, D. Natelson and J. C. Cuevas, *Phys. Rev. B*, 2011, **83**, 193404.
- 20 E. Hao and G. C. Schatz, *The Journal of Chemical Physics*, 2004, **120**, 357–366.
- 21 I. Romero, J. Aizpurua, G. W. Bryant and F. J. García de Abajo, *Opt. Express*, 2006, **14**, 9988–9999.
- 22 P. K. Jain and M. A. El-Sayed, *Chemical Physics Letters*, 2010, **487**, 153–164.
- 23 M. Danckwerts and L. Novotny, *Phys. Rev. Lett.*, 2007, **98**, 026104.
- 24 M. Kauranen and A. V. Zayats, *Nature Photonics*, 2012, **6**, 737–748.
- 25 M. Scalora, M. A. Vincenti, D. de Ceglia and J. W. Haus, [arXiv:1405.6999 \[physics.optics\]](https://arxiv.org/abs/1405.6999), 2014.
- 26 P. J. Schuck, D. P. Fromm, A. Sundaramurthy, G. S. Kino and W. E. Moerner, *Phys. Rev. Lett.*, 2005, **94**, 017402.
- 27 A. I. Fernández-Domínguez, S. A. Maier and J. B. Pendry, *Phys. Rev. Lett.*, 2010, **105**, 266807.
- 28 L. Yang, H. Wang, B. Yan and B. M. Reinhard, *The Journal of Physical Chemistry C*, 2010, **114**, 4901–4908.
- 29 T. Atay, J.-H. Song and A. V. Nurmikko, *Nano Letters*, 2004, **4**, 1627–1631.
- 30 S. Marhaba, G. Bachelier, C. Bonnet, M. Broyer, E. Cottancin, N. Grillet, J. Lermé, J.-L. Vialle and M. Pellarin, *The Journal of Physical Chemistry C*, 2009, **113**, 4349–4356.
- 31 S. S. Acimović, M. P. Kreuzer, M. U. González and R. Quidant, *ACS Nano*, 2009, **3**, 1231–1237.
- 32 K.-H. Su, Q.-H. Wei, X. Zhang, J. J. Mock, D. R. Smith and S. Schultz, *Nano Letters*, 2003, **3**, 1087–1090.
- 33 O. Pérez-González, N. Zabala, A. G. Borisov, N. J. Halas, P. Nordlander and J. Aizpurua, *Nano Letters*, 2010, **10**, 3090–3095.
- 34 D. C. Marinica, A. K. Kazansky, P. Nordlander, J. Aizpurua and A. G. Borisov, *Nano Letters*, 2012, **12**, 1333–1339.
- 35 Z. Jacob and V. M. Shalav, *Science*, 2011, **334**, 463–464.
- 36 M. S. Tame, K. R. McEnery, Ş. K. Özdemir, J. Lee, S. A. Maier and M. S. Kim, *Nat Phys*, 2013, **9**, 329–340.
- 37 U. Kreibitz and M. Vollmer, *Optical Properties of Metal Clusters*, Springer, 1995.
- 38 S. Berciaud, L. Cognet, P. Tamarat and B. Lounis, *Nano Letters*, 2005, **5**, 515–518.
- 39 J. Tiggesbäumker, L. Köller, K.-H. Meiwes-Broer and A. Liebsch, *Phys. Rev. A*, 1993, **48**, R1749–R1752.
- 40 S. Fedrigo, W. Harbich and J. Buttet, *Phys. Rev. B*, 1993, **47**, 10706–10715.
- 41 L. B. Scaffardi, N. Pellegrini, O. de Sanctis and J. O. Tocho, *Nanotechnology*, 2005, **16**, 158–163.
- 42 E. Cottancin, G. Celep, J. Lermé, M. Pellarin, J. Huntzinger, J. Vialle and M. Broyer, *Theoretical Chemistry Accounts*, 2006, **116**, 514–523.
- 43 J. Lermé, B. Palant, B. Prével, M. Pellarin, M. Treilleux, J. L. Vialle, A. Perez and M. Broyer, *Phys. Rev. Lett.*, 1998, **80**, 5105–5108.
- 44 V. V. Kresin, *Phys. Rev. B*, 1995, **51**, 1844–1849.
- 45 J. A. Scholl, A. L. Koh and J. A. Dionne, *Nature*, 2012, **483**, 421–427.
- 46 K. J. Savage, M. M. Hawkeye, R. Esteban, A. G. Borisov, J. Aizpurua and J. J. Baumberg, *Nature*, 2012, **491**, 574–577.
- 47 C. Ciraci, R. T. Hill, J. J. Mock, Y. Urzhumov, A. I. Fernández-Domínguez, S. A. Maier, J. B. Pendry, A. Chilkoti and D. R. Smith, *Science*, 2012, **337**, 1072–1074.
- 48 D.-K. Lim, K.-S. Jeon, J.-H. Hwang, H. Kim, S. Kwon, Y. D. Suh and J.-M. Nam, *Nat Nano*, 2011, **6**, 452–460.
- 49 R. W. Taylor, T.-C. Lee, O. A. Scherman, R. Esteban, J. Aizpurua, F. M. Huang, J. J. Baumberg and S. Mahajan, *ACS Nano*, 2011, **5**, 3878–3887.
- 50 D. R. Ward, N. K. Grady, C. S. Levin, N. J. Halas, Y. Wu, P. Nordlander and D. Natelson, *Nano Letters*, 2007, **7**, 1396–1400.
- 51 J.-S. Huang, V. Callegari, P. Geisler, C. Brüning, J. Kern, J. C. Prangsma, X. Wu, T. Feichtner,

- J. Ziegler, P. Weinmann, M. Kamp, A. Forchel, P. Biagioni, U. Sennhauser and B. Hecht, *Nat Commun*, 2010, **1**, 150.
- 52 J. Kern, S. Großmann, N. V. Tarakina, T. Häckel, M. Emmerling, M. Kamp, J.-S. Huang, P. Biagioni, J. C. Prangma and B. Hecht, *Nano Letters*, 2012, **12**, 5504–5509.
- 53 S. F. Tan, L. Wu, J. K. Yang, P. Bai, M. Bosman and C. A. Nijhuis, *Science*, 2014, **343**, 1496–1499.
- 54 H. Cha, J. H. Yoon and S. Yoon, *ACS Nano*, 2014, **8**, 8554–8563.
- 55 W. Zhu, *Plasmonics for surface-enhanced Raman scattering: from classical to quantum*, PhD Thesis, Harvard University, 2014.
- 56 J. Zuloaga, E. Prodan and P. Nordlander, *ACS Nano*, 2010, **4**, 5269–5276.
- 57 R. E. Stratmann, G. E. Scuseria and M. J. Frisch, *J. Chem. Phys.*, 1998, **109**, 8218–8224.
- 58 M. A. L. Marques and E. K. U. Gross, *Annual Review of Physical Chemistry*, 2004, **55**, 427–455.
- 59 L. Mao, Z. Li, B. Wu and H. Xu, *Applied Physics Letters*, 2009, **94**, 243102.
- 60 J. Zuloaga, E. Prodan and P. Nordlander, *Nano Letters*, 2009, **9**, 887–891.
- 61 P. Song, P. Nordlander and S. Gao, *J. Chem. Phys.*, 2011, **134**, 074701.
- 62 R. Esteban, A. G. Borisov, P. Nordlander and J. Aizpurua, *Nat Commun*, 2012, **3**, 825.
- 63 P. Zhang, J. Feist, A. Rubio, P. García-González and F. J. García-Vidal, [arXiv:1403.8016v1](https://arxiv.org/abs/1403.8016v1), 2014.
- 64 R. Ruppin, *J. Opt. Soc. Am.*, 1976, **66**, 449–453.
- 65 R. Fuchs and K. L. Kliewer, *Phys. Rev. B*, 1971, **3**, 2270–2278.
- 66 P. J. Feibelman, *Phys. Rev. B*, 1975, **12**, 1319–1336.
- 67 B. B. Dasgupta and R. Fuchs, *Phys. Rev. B*, 1981, **24**, 554–561.
- 68 W. L. Mochán, R. Fuchs and R. G. Barrera, *Phys. Rev. B*, 1983, **27**, 771–780.
- 69 R. Fuchs and F. Claro, *Phys. Rev. B*, 1987, **35**, 3722–3727.
- 70 R. Rojas, F. Claro and R. Fuchs, *Phys. Rev. B*, 1988, **37**, 6799–6807.
- 71 R. Ruppin, *J. Opt. Soc. Am. B*, 1989, **6**, 1559–1563.
- 72 A. Liebsch and W. L. Schaich, *Phys. Rev. B*, 1995, **52**, 14219–14234.
- 73 A. Liebsch, *Phys. Rev. B*, 1993, **48**, 11317–11328.
- 74 I. A. Larkin, M. I. Stockman, M. Achermann and V. I. Klimov, *Phys. Rev. B*, 2004, **69**, 121403.
- 75 P. Johansson, H. Xu and M. Käll, *Phys. Rev. B*, 2005, **72**, 035427.
- 76 J. Aizpurua and A. Rivacoba, *Phys. Rev. B*, 2008, **78**, 035404.
- 77 F. J. García de Abajo, *The Journal of Physical Chemistry C*, 2008, **112**, 17983–17987.
- 78 J. M. McMahon, S. K. Gray and G. C. Schatz, *Phys. Rev. Lett.*, 2009, **103**, 097403.
- 79 J. M. McMahon, S. K. Gray and G. C. Schatz, *Nano Letters*, 2010, **10**, 3473–3481.
- 80 C. David and F. J. García de Abajo, *The Journal of Physical Chemistry C*, 2011, **115**, 19470–19475.
- 81 G. Toscano, S. Raza, A.-P. Jauho, N. A. Mortensen and M. Wubs, *Opt. Express*, 2012, **20**, 4176–4188.
- 82 S. Raza, N. Stenger, S. Kadkhodazadeh, S. V. Fischer, N. Kotesha, A.-P. Jauho, A. Burrows, M. Wubs and N. A. Mortensen, *Nanophotonics*, 2013, **2**, 131–138.
- 83 L. Stella, P. Zhang, F. J. García-Vidal, A. Rubio and P. García-González, *The Journal of Physical Chemistry C*, 2013, **117**, 8941–8949.
- 84 N. A. Mortensen, S. Raza, M. Wubs, T. Søndergaard and S. I. Bozhevolnyi, *Nat Commun*, 2014, **5**, 3809.
- 85 A. I. Fernández-Domínguez, A. Wiener, F. J. García-Vidal, S. A. Maier and J. B. Pendry, *Phys. Rev. Lett.*, 2012, **108**, 106802.
- 86 T. V. Teperik, P. Nordlander, J. Aizpurua and A. G. Borisov, *Opt. Express*, 2013, **21**, 27306–27325.
- 87 T. V. Teperik, P. Nordlander, J. Aizpurua and A. G. Borisov, *Phys. Rev. Lett.*, 2013, **110**, 263901.
- 88 Y. Luo, A. I. Fernandez-Dominguez, A. Wiener, S. A. Maier and J. B. Pendry, *Phys. Rev. Lett.*, 2013, **111**, 093901.
- 89 G. Toscano, C. Rockstuhl, F. Evers, H. Xu, N. A. Mortensen and M. Wubs, [arXiv:1408.5862 \[physics.optics\]](https://arxiv.org/abs/1408.5862), 2014.
- 90 J. A. Scholl, A. García-Etxarri, A. L. Koh and J. A. Dionne, *Nano Letters*, 2013, **13**, 564–569.
- 91 T. Dong, X. Ma and R. Mittra, *Applied Physics Letters*, 2012, **101**, 233111.

-
- 92 E. Townsend and G. W. Bryant, *Nano Letters*, 2012, **12**, 429–434.
- 93 W. Ekardt, *Phys. Rev. B*, 1985, **31**, 6360–6370.
- 94 W. A. de Heer, P. Milani and A. Châtelain, *Phys. Rev. Lett.*, 1989, **63**, 2834–2836.
- 95 P.-A. Hervieux and J.-Y. Bigot, *Phys. Rev. Lett.*, 2004, **92**, 197402.
- 96 E. Prodan, P. Nordlander and N. J. Halas, *Nano Letters*, 2003, **3**, 1411–1415.
- 97 H. Winter, *Physics Reports*, 2002, **367**, 387 – 582.
- 98 N. D. Lang and P. Avouris, *Nano Letters*, 2002, **2**, 1047–1050.
- 99 Th. Fennel, K.-H. Meiwes-Broer, J. Tiggesbäumker, P.-G. Reinhard, P. M. Dinh and E. Surraud, *Rev. Mod. Phys.*, 2010, **82**, 1793–1842.
- 100 F. Krausz and M. Ivanov, *Rev. Mod. Phys.*, 2009, **81**, 163–234.
- 101 O. I. Tolstikhin and T. Morishita, *Phys. Rev. A*, 2012, **86**, 043417.
- 102 V. S. Popov, *Physics-Uspekhi*, 2004, **47**, 855–885.
- 103 A. Zugarramurdi, N. Zabala, A. G. Borisov and E. V. Chulkov, *Phys. Rev. B*, 2011, **84**, 115422.
- 104 E. V. Chulkov, V. M. Silkin and P. M. Echenique, *Surface Science*, 1999, **437**, 330 – 352.
- 105 J. M. Pitarke, F. Flores and P. M. Echenique, *Surface Science*, 1990, **234**, 1 – 16.
- 106 J. M. Blanco, F. Flores and R. Pérez, *Progress in Surface Science*, 2006, **81**, 403 – 443.
- 107 V. M. Silkin, J. Zhao, F. Guinea, E. V. Chulkov, P. M. Echenique and H. Petek, *Phys. Rev. B*, 2009, **80**, 121408.
- 108 D. Ferry and S. Goodnick, *Transport in nanostructures*, Crambridge University Press, 1999.
- 109 J. D. Jackson, *Classical Electrodynamics*, 3rd edition, John Wiley, NY, 1998.
- 110 J. W. Haus, D. de Ceglia, M. A. Vincenti and M. Scalora, *JOSA B*, 2014, **31**, 259–269.
- 111 J. W. Haus, D. de Ceglia, M. A. Vincenti and M. Scalora, *JOSA B*, 2014, **31**, A13–A19.
- 112 P. K. Tien and J. P. Gordon, *Phys. Rev.*, 1963, **129**, 647–651.
- 113 P. B. Johnson and R. W. Christy, *Phys. Rev. B*, 1972, **6**, 4370–4379.
- 114 B. Hetényi, F. De Angelis, P. Giannozzi and R. Car, *The Journal of Chemical Physics*, 2001, **115**, year.
- 115 F. J. García de Abajo and A. Howie, *Phys. Rev. B*, 2002, **65**, 115418.
- 116 A. Eguluz, S. C. Ying and J. J. Quinn, *Phys. Rev. B*, 1975, **11**, 2118–2121.
- 117 J. M. Pitarke, V. M. Silkin, E. V. Chulkov and P. M. Echenique, *Reports on Progress in Physics*, 2007, **70**, 1–87.
- 118 P. Nordlander, C. Oubre, E. Prodan, K. Li and M. I. Stockman, *Nano Letters*, 2004, **4**, 899–903.
- 119 W. Rechberger, A. Hohenau, A. Leitner, J. R. Krenn, B. Lamprecht and F. R. Aussenegg, *Optics Communications*, 2003, **220**, 137 – 141.
- 120 H. Xu, J. Aizpurua, M. Käll and P. Apell, *Phys. Rev. E*, 2000, **62**, 4318–4324.
- 121 J. B. Lassiter, J. Aizpurua, L. I. Hernandez, D. W. Brandl, I. Romero, S. Lal, J. H. Hafner, P. Nordlander and N. J. Halas, *Nano Letters*, 2008, **8**, 1212–1218.
- 122 A. Aubry, D. Y. Lei, A. I. Fernández-Domínguez, Y. Sonnefraud, S. A. Maier and J. B. Pendry, *Nano Letters*, 2010, **10**, 2574–2579.
- 123 A. I. Fernández-Domínguez, P. Zhang, Y. Luo, S. A. Maier, F. J. García-Vidal and J. B. Pendry, *Phys. Rev. B*, 2012, **86**, 241110.
- 124 R. C. Monreal, T. J. Antosiewicz and S. P. Apell, *New Journal of Physics*, 2013, **15**, 083044.
- 125 M. Schnell, A. García Etxarri, A. J. Huber, K. Crozier, J. Aizpurua and R. Hillenbrand, *Nat Photon*, 2009, **3**, 287–291.
- 126 R. Esteban, G. Aguirregabiria, A. G. Borisov et al, in preparation.
- 127 L. Wu, H. Duan, P. Bai, M. Bosman, J. K. W. Yang and E. Li, *ACS Nano*, 2013, **7**, 707–716.
- 128 D. R. Ward, F. Hüser, F. Pauly, J. C. Cuevas and D. Natelson, *Nat Nano*, 2010, **5**, 732–736.
- 129 A. Stolz, J. Berthelot, M.-M. Mennemanteuil, G. Colas des Francs, L. Markey, V. Meunier and A. Bouhelier, 2014, **14**, 2330–2338.